INVESTIGATION OF AN OPTICALLY CREATED DEAD ZONE BY LOW-ONE PHOTON POLYMERIZATION FOR SILICONE STEREOLITHOGRAPHY

A Dissertation

by

DONG SUNG KIM

Submitted to the Office of Graduate and Professional Studies of
Texas A&M University
in partial fulfillment of the requirements for the degree of

DOCTOR OF PHILOSOPHY

Chair of Committee,	Bruce L. Tai
Committee Members,	Jyhwen Wang
	Melissa Grunlan
	Chao Ma
Head of Department,	Andreas Polycarpou

December 2019

Major Subject: Mechanical Engineering

ABSTRACT

Silicones have a variety of applications in many fields because of their unique properties such as bio-applicable, corrosion resistive, mechanically elastic and tough, and stable under a high temperature condition. 3D printing techniques have been actively studied freedom to fabricate complex geometries. Vat photopolymerization (VP) provides a high printing resolution, better mechanical isotropy, minimal structure defects, and fine surface finish.

This study evaluated the printability of the silicone photopolymer with digital light processing. The results showed a good dimensional accuracy and better mechanical isotropy. However, it was found that the strong adhesion between the cured polymer and the bottom surface of a vat. The separation force to overcome the adhesion caused a slow printing speed and printing failures.

To eliminate the separation force, an optical method to create a gap between the interface was investigated. Using a low one-photon polymerization (LOPP), a limited curing at the focal spot was successfully demonstrated. Three different wavelengths with different absorbance rates were selected and tested under the stationary and moving exposure conditions. the ultra-low absorbance wavelength showed a higher printing resolution and lower geometrical variation. With a small error, the data from the stationary exposure condition converted to the parameter for the moving exposure condition. However, it also found that the ultra-low absorbance wavelength required extremely high irradiance to compensate the time loss from its ultra-low absorbance. The

time could not be linearly scaled by power due to the non-steady state polymerization kinetics.

DEDICATION

To my beloved family for encouraging me and supporting me as always. To my advisor, Dr. Bruce Tai, for making me confident and optimistic.

ACKNOWLEDGEMENTS

I would like to thank the committee chair, Dr. Bruce Tai and the committee members, Dr. Jyhwen Wang, Dr. Melissa Grunlan, Dr. Chao Ma for their guidance and support throughout the process of this research.

Thanks also go to my friends and colleagues and the department faculty and staff for making my time at Texas A&M University a great experience.

Lastly, thanks to my Kids, Joohwan and Yehwan for their love and to my wife, Jin Soo for her sacrifice and love.

CONTRIBUTORS AND FUNDING SOURCES

Contributors

This work was supervised by a dissertation committee consisting of Assistant Professor Dr. Bruce Tai (Advisor) of the Department of Mechanical Engineering, Professor Dr. Jyhwen Wang of the Department of Engineering Technology and Industrial Distribution, Professor Dr. Melissa Grunlan of the Department of Biomedical Engineering, and Assistant Professor Dr. Chao Ma of the Department of Engineering Technology and Industrial Distribution. Part of the experiments in this dissertation was assisted by the members of the Manufacturing Innovation Lab.

Funding Sources

This study was supported by funding provided by NSF grant #1522877. Its contents are solely the responsibility of the authors and do not necessarily represent the official views of the NSF.

TABLE OF CONTENTS

Page

LIST OF FIGURES

Page

LIST OF TABLES

1. INTRODUCTION

1.1. Background

Additive manufacturing (also known as 3D printing) technologies have been improved to fabricate three-dimensional structures with a variety of materials. In general, stiff and rigid source materials such as metals, ceramics, and plastics have been used. Recent advancements have made it possible to print flexible, rubber-like polymers and even gradient materials by mixing different ratios of polymer resins. Applications have also been expanded from prototypes to functional parts. However, 3D Printing still cannot substitute for the conventional fabrication techniques due to the limitations of surface finish, tolerances, or material selection. Another challenge is printing soft materials such as silicones, because of the low shape stability [1]. The printed structures can collapse or deform during, or even after the printing due to low stiffness and high density.

Silicone materials have many applications in medical simulators [2], tissue-engineering structures [3] and soft robotics [4]. Molding process or soft lithography is a common technique to shape soft materials [5]. However, these methods can have physical limitations such as creating enclosed cavities, internal channel, or complex 3D features. Alternatively, 3D printing techniques may be utilized to overcome these issues in silicone 3D printing. However, the conventional 3D printing processes could have the other challenges. For example, one of the popular 3D printing processes, an extrusion-based process has some issues such as structural defects and rough surface finish.

Vat photopolymerizaion (VP) such as stereolithography (SLA), digital light process (DLP) can overcome the issues with the ones of the extrusion-based process, but the separation issue is critical in vat photopolymerizaion which occur from the adhesion between a cured polymer and the bottom surface of a vat that has a significant bonding force [6]. To solve the separation issue, researchers have investigated various methods, including a non-stick coating in the interface, detaching motions, and chemical inhibition phenomena.

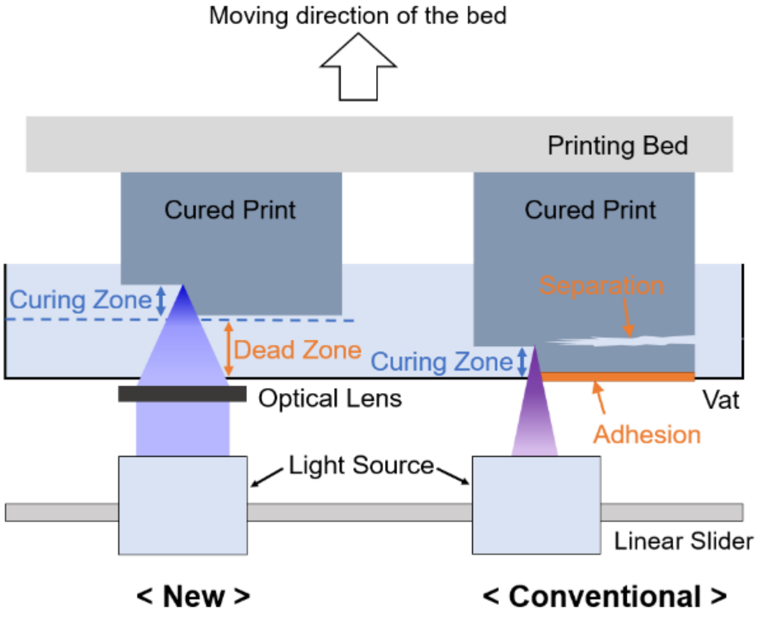

Figure 1. Comparison of the proposed and conventional VP process.

The objective of this dissertation is to investigate a new 3D printing process to solve the separation issue by creating an optical deadzone for silicone photopolymer as shown in Figure 1. A feasibility study was conducted to verify the printability of the silicone photopolymer with a commercial DLP printer. A testbed for the dead zone process was designed and built to verify the dead zone formation and to characterize the printing performance. In details, two sets of experiments for stationary and moving exposure conditions were conducted with different process parameters and also analyzed the data to evaluate the behaviors under the dead zone process. An irradiance model was developed to analyze the data between the stationary and moving exposure test.

1.2. Literature Review

Silicone materials have broad applications ranging from tissue engineering to soft robotics. Researchers have studied the printing of the materials, but these works are mostly limited to the extrusion-based process [7]. The extrusion-based process utilizes a nozzle or a syringe to extrude material to form a three-dimensional object. Due to the relatively simple system components, this process is common to realize a 3D printing process. Commercial 3D printers with the process have been released such as Bioplotter (Envision Tech), Silicone 3D printer (Picsima), and ACEO Imagine printer (Wacker). Bioplotter and Picsima printer both use a two-part silicone and syringe extruder to form three-dimensional parts. ACEO printer uses UV-curable silicone and the drop-on-demand technology. These printers can print soft materials like silicones but may not handle complex structures or fine features due to the low shape stability. Plott et al. [8] demonstrated the extrusion-based printing with moisture-cure silicone elastomer for pneumatic actuators. Even though they fabricated soft structures with a simple system, a number of drawbacks including structural defects, low dimensional accuracy, mechanical anisotropy, nozzle clogging, and poor surface finish [8, 22, 24].

Vat photopolymerization (VP) of silicone can produce better finish and higher resolution than the conventional extrusion-based method. Au et al. reported stereolithography (SLA) with an UV-curable silicone for the preparation of microfluidic devices [9]. Bhattacharjee et al. developed an UV-curable silicone for digital light processing (DLP) that matches the properties of the commercial PDMS Sylgard-184 [10]. However, their silicone takes longer time (several seconds) to cure than the time used in DLP/SLA with commercial acrylate photopolymers. In addition to the material itself, another major obstacle to SLA and DLP of silicones and other polymers is separation [11-13], occurring from the adhesion between a cured polymer and the vat bottom that has a significant bonding force [6]. To solve the separation issue, researchers have investigated various methods, including a non-stick coating in the interface, detaching motions, ultrasonic vibration, and chemical inhibition phenomena. Commonly, a Teflon sheet (or silicone for non-silicone resins) is used at the bottom of a vat as a non-stick layer and a detaching motion is applied after each layer of print to separate the cured part from the vat [6, 13, 14]. However, the non-stick sheet needs to be replaced regularly, and the detaching motion increases the total printing time and also could make any damages on the surface. Tumbleston et al. demonstrated a DLP process with oxygen inhibition phenomenon [15]. The bottom of a vat has an oxygen-permeable window. Oxygen gas molecules diffuse through the window to create a “dead zone” at the interface of the vat and a cured part. Although the oxygen-induced dead zone can effectively eliminate the separation problem and speed up the printing time, it is only applicable (and sensitive) to specific photopolymers with free radical polymerization. Further, gas diffusion often results in a non-uniform thickness of the dead zone, which makes it difficult to print a solid and flat surface [16]. Another constraint of this approach is the limited manufacturable size of the permeable window.

Herein, this study suggests a new dead zone process free to the type of the photopolymer and the gas diffusion issue and the limited window size.

1.3. Research Objectives

The objective of this research is to explore the feasibility of an optically created dead zone process for silicone 3D printing. An in-house Polydimethylsiloxane (PDMS) will be synthesized to get a controlled material. A testbed for the new dead zone process will be designed and built to characterize the process. An irradiance model will be developed to understand two different exposure conditions with process parameters. The ultimate goal of this research is to evaluate the dead zone process and to find the optimal process condition.

1.4. Organization of the Dissertation

This dissertation follows the regular journal format. Each section has abstract, introduction, materials & methods, results, discussions, and conclusions. Section 2 discusses the experimental study of silicone 3D printing with DLP process. Section 3 presents a feasibility study of silicone stereolithography with an optically created dead zone. Section 4 details the experimental study of a high-power beam of a long wavelength and also the modeling results with a Gaussian beam distribution. In the end, section 5 concludes the dissertation and propose future works for this topic.

2. PRINTABILITY OF SILICONE USING DIGITAL LIGHT PROCESSING

2.1. Abstract

This section investigates the printability of Polydimethylsiloxane (PDMS) photopolymer with digital light processing (DLP) in terms of dimensional accuracy, mechanical properties, isotropy, and postcure shrinkage. The controlled PDMS photopolymer was made from a methacrylated PDMS-macromer and TPO-L photoinitiator. The PDMS was printed using different orientations, sizes, and post-exposure conditions and then evaluated by tensile test and microscope to verify the printability. In general, printed parts showed good dimensional accuracy and low shrinkage, but high directionality in modulus, ductility and strength. The dimensional error is less than 2% and the shrinkage rates are less than 0.52%. In contrast, the modulus varies between 0.87 and 0.96 MPa depending on print orientation, elongation varies from 34.7% to 66.4%, and strength varies from 0.23 to 0.49 MPa. The separation issue was also observed with the PDMS during the printing. Additional support structures were added to increase structural strength against the separation force.

2.2. Introduction

Polydimethylsiloxane (PDMS) is a widely used silicone-based polymer because of its mechanical properties, optical transparency, bio-friendly, and corrosion and temperature resistance. Molding and soft lithography are common fabrication methods for PDMS [17, 18], but these methods cannot produce complex geometries such as open cellular or internal structures [19, 20]. The emergence of 3D printing provides alternative means to build complex parts from a digital model with a variety of polymer options; however, use of PDMS has not been well documented in the literature. Recent advancements in silicone 3D printing focus on extrusion-based methods [8, 21-23]. Extrusion-based methods have a number of drawbacks including structural defects, low dimensional accuracy, mechanical anisotropy, nozzle clogging, and poor surface finish [8, 22, 24]. On the other hand, vat photopolymerizaion (VP), such as stereolithography (SLA) and digital light processing (DLP), is known to produce parts with minimal structure defects, high printing resolution, better mechanical isotropy, and fine surface finish [25-27]. However, only a few studies on silicone VP can be found and they focus on application and development rather than the process itself. For example, Au et al. used SLA and an UV-curable silicone to manufacture microfluidic devices [9]. Bhattacharjee et al. developed an UV-curable silicone for DLP that could match the properties of the commercial PDMS Sylgard-184 [10].

Although VP has advantages over extrusion-based methods, there are other issues including separation issues and postcure shrinkage [27-29]. Separation issues are caused by the strong adhesion between the cured polymer and the bottom surface of a vat [11, 13], which can lead to printing failure, slow printing speed, and poor surface finish. Postcure shrinkage occurs during the post exposure and is aided by insufficient polymerization during printing. The shrinkage lowers dimensional accuracy and sometimes causes part distortion and breakage [30]. Additionally, printed parts usually do not have equal strength in all directions. Dulieu-Barton et al. found that parts printed by SLA with an epoxy-based resin showed anisotropy with printing orientations [26]. Monzon et al. reported that the pixilation of a digital micromirror device (DMD) produced anisotropy of parts printed by DLP with acrylated resins [31]. Small areas between each pixel in DMD provided a poor level of curing of the materials which caused defects, such as small holes, in the part. The vertical printing orientation showed better mechanical behavior than the horizontal directions.

To understand the VP printability of PDMS, this study is focused on three printing criteria: dimensional accuracy, mechanical isotropy, and postcure shrinkage. Photo-curable PDMS was synthesized in house because of limited options in commercially available products. Also, commercial products often contain solvent or additives which are extraneous variables in the experiment. For the printing test, a conventional DLP printer that grants parameter access was used, allowing for proper exposure settings for the PDMS resin to be found. The experimental methods, materials, and results are detailed in the following sections.

2.3. Materials and Methods

2.3.1. Preparations for Material Printing

A methacrylated PDMS-macromer was synthesized via triflic acid-catalyzed ring-opening polymerization of octamethylcyclotetrasiloxane (D_4) and 1,3-bis(3-methacryloxypropyl) tetramethyldisiloxane, a methacrylate end-capping agent. The detailed synthesis procedure follows the work published elsewhere [32], and results in a transparent liquid. Figure 2 (a) shows the chemical structure of the synthesized PDMS-macromer. The material has an average molecular weight (Mn) of 5600 g/mol, viscosity of 109 cP and glass transition temperature (Tg) of -124°C.

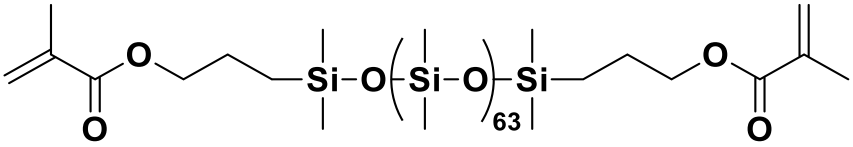

(a)

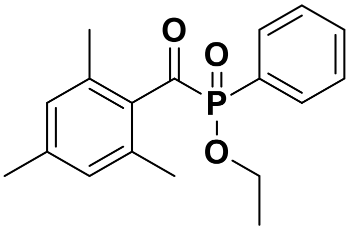

(b)

Figure 2. The chemical structures of (a) the synthesized PDMS-macromer and (b) TPO-L photoinitiator.

Ethyl (2,4,6-trimethylbenzoyl) phenyl phosphinate, a clear yellowish liquid, was used as a photoinitiator (Combi-Blocks Inc., San Diego, CA), also known as TPO-L. Figure 2 (b) shows the chemical structure of the photoinitiator. The characteristic peak of the photoinitiator is at 370 nm in an UV-vis absorption spectrum. TPO-L of 2 wt.% was added to the PDMS macromer, which is considered the maximum solubility for this system [33]. Without any solvent, the PDMS-macromer and TPO-L were mixed by DAC150 SpeedMixer at 3500 RPM for 2 min (FlackTek Inc., Landrum, SC).

A commercial DLP 3D printer, Nobel Superfine, was used in this study (XYZprinting, New Taipei City, Taiwan). The printer has a print dimension of 64 mm × 40 mm × 120 mm, X-Y resolution of 50 μm, and layer resolution (Z-axis) of 25 μm. Prior to the printing experiment, parametric studies were conducted to tune the machine specifically for the PDMS used. A long exposure time of at least 10 s (vs. few milliseconds for acrylated resins) was needed to cure the material. A slow peeling speed (0.0625 mm/s) was used to mitigate material damage during separation. The final printing parameters were verified with various test prints as shown in Figure 3. The printed parts were washed with isopropyl alcohol with concentration of 99% for 15 minutes and dried at room temperature.

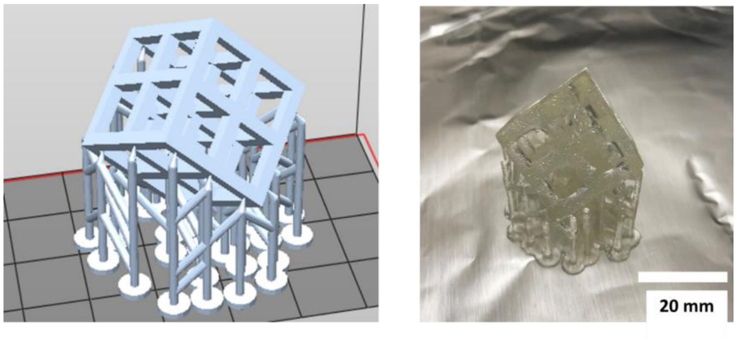

(a)

Figure 3. Test printing with various geometries: (a) lattice structure, (b) spring, (c) nasal prosthesis. The top row shows the digital models and the bottom row shows the actual printed parts.

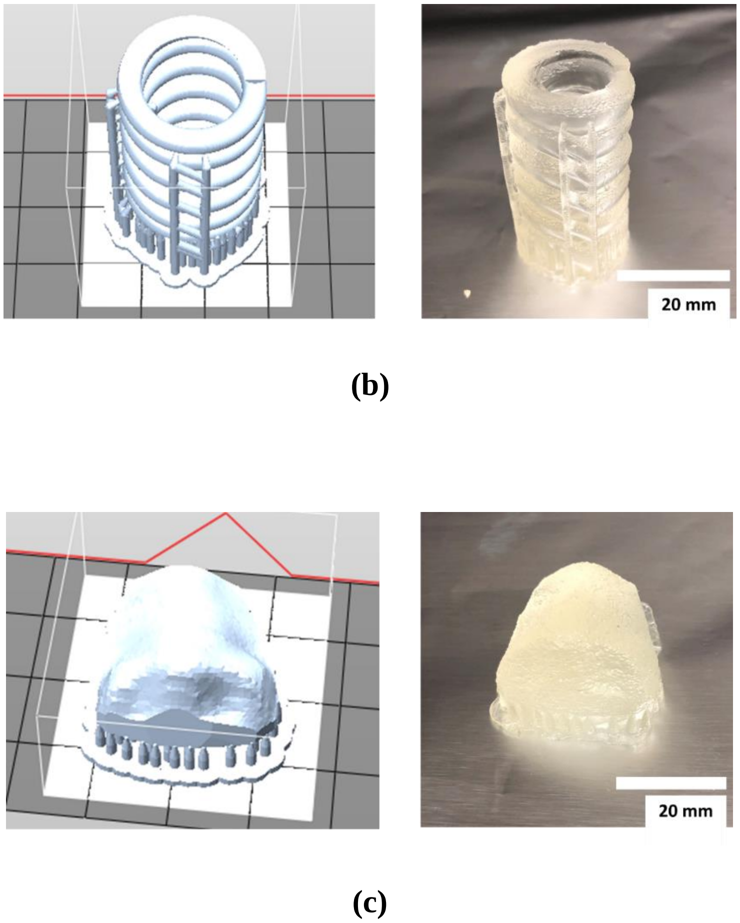

(b)

(c)

Figure 3 Continued.

2.3.2. Methods

This study used three different printing orientations as shown in Figure 4 (a). In the X orientation, the width and longitudinal sides of a specimen are perpendicular to the layering direction. In the Y orientation, the edge and longitudinal sides of the specimen are perpendicular to the layering. The Z orientation has the edge and width sides perpendicular to the layering. For evaluating dimensional accuracy, three 20-mm cubes were printed without post exposure, as shown in Figure 4 (b). They were then measured by a microscope with 0.01 mm resolution (Dino-Lite, Torrance, CA) because other contact methods of measurement can deform the soft PDMS. A total of 27 data points was obtained, nine points per orientation. Regarding mechanical isotropy, tensile test specimens with three different printing orientations were considered as shown in Figure 4 (a). A total of 18 specimens were printed with six specimens per orientation. The mechanical properties of interest were the modulus of elasticity, elongation, and ultimate tensile strength which were obtained by a universal testing system (Instron, Norwood, MA) following ASTM D638 standard. The size of the specimens was scaled down to 60% of the standard due to the limited size of the printing bed. For post-cure shrinkage, three different sizes of cubes were printed with 10 mm, 15 mm, and 20 mm lengths, respectively, as shown in Figure 4 (c). The dimensions of cubes were measured by the microscope before and after postcuring. The postcuring was conducted using a UV transilluminator of a radiant power of 3.1 mW/cm^2 and exposure time of 60 minutes at room temperature (UVP, Upland, CA). A total of 108 data points was obtained with 36 points per cube.

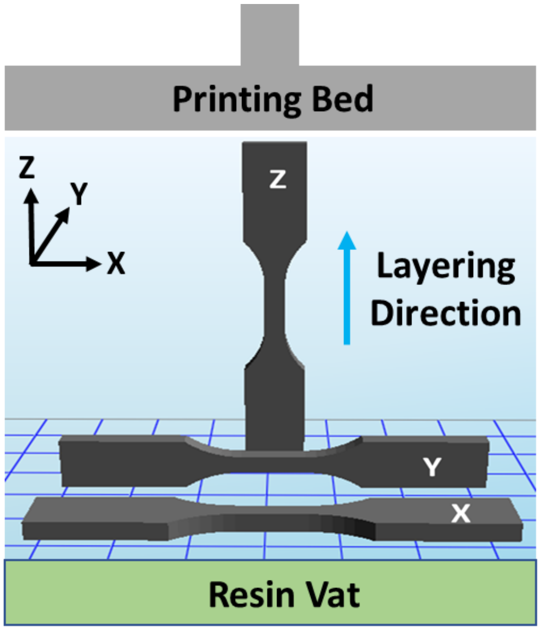

(a)

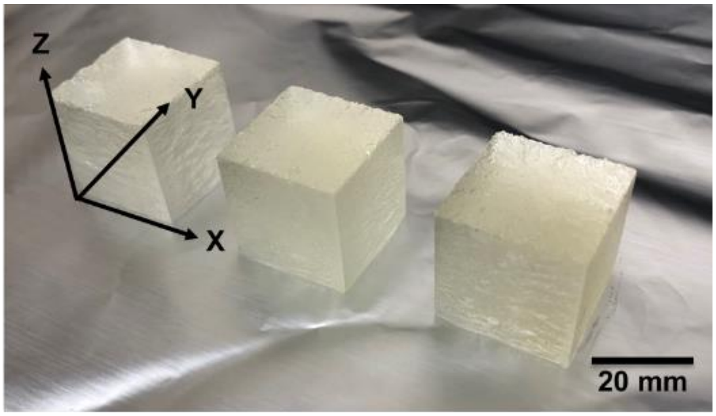

(b)

Figure 4. Specimens for printability studies: (a) printing orientations of specimens for mechanical isotropy test, (b) 20 mm cubes for evaluating dimensional accuracy, and (c) cubes of three different sizes for determining postcure shrinkage.

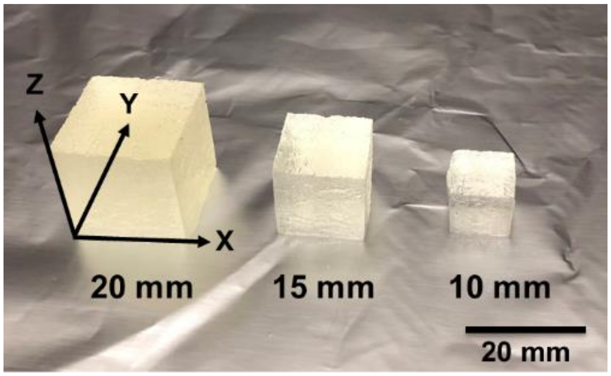

(c)

Figure 4 Continued.

2.4. Results and Discussion

2.4.1. Dimensional Accuracy

Figure 5 shows the measured dimensions in X, Y, and Z directions of the 20-mm cubes with an error bar representing the standard error. The average lengths in Z and Y directions are shorter than the desired length of 20 mm, while the X direction length exceeds this. This is likely because the metal surface of the printing bed reflects the incident UV light, which may result in slight over curing and therefore greater length; however, the overall errors are fairly small, ranging from 0.6% to 2.0%. This range indicates higher accuracy when compared to the typical 1.25% to 6.21% error of commercial resins [34]. The Z-direction demonstrates the best accuracy due to a finer resolution of 25 μm as opposed to the 50 μm X-Y resolution of the printer.

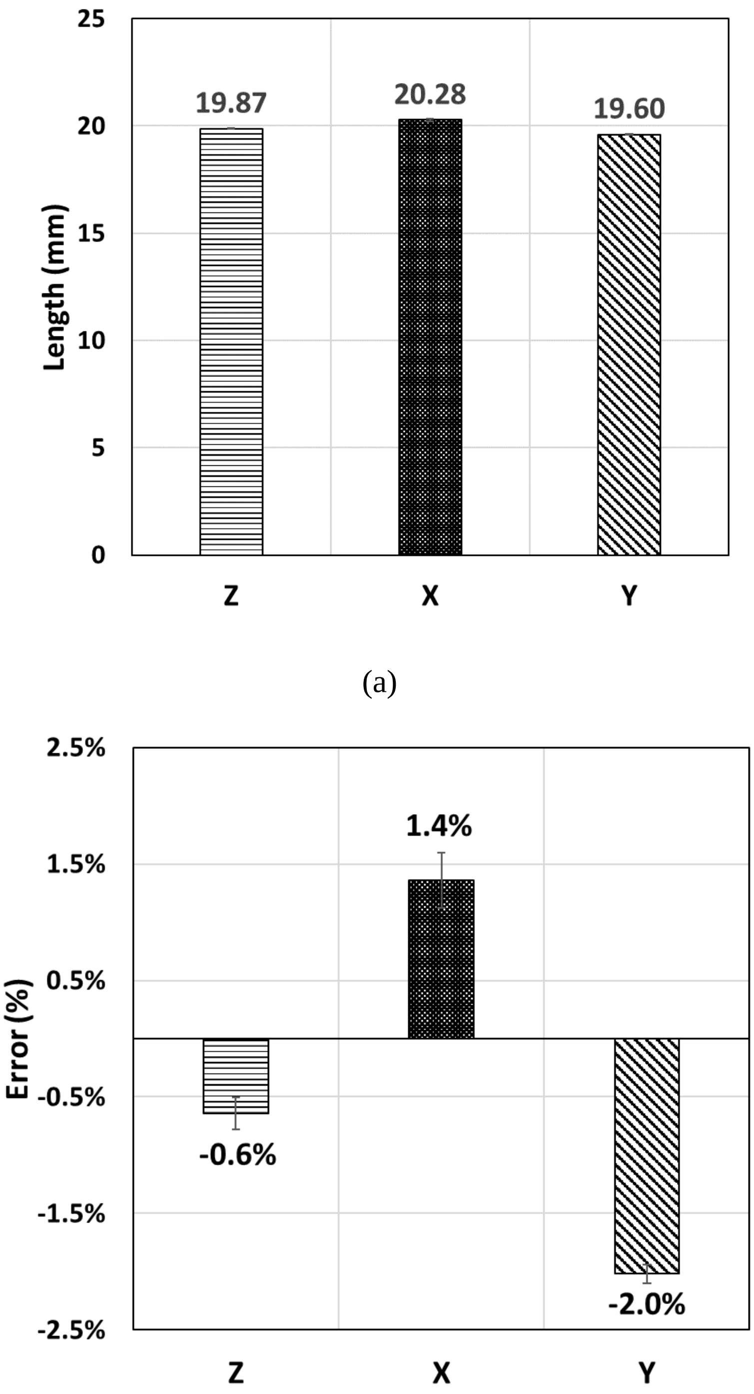

Figure 5. Results for dimensional accuracy in X, Y, and Z directions: (a) measured length in each direction and (b) percent error based on the 20 mm nominal size.

2.4.2. Mechanical Isotropy

Figure 6 shows the results for the modulus of elasticity, elongation, and ultimate tensile strength in three printing orientations. The error bars represent the standard error. All of the data was analyzed with one-way analysis of variance (ANOVA) with a p-value < 0.05 for statistical significance and followed by post-hoc Tukey-Kramer Honest Significant Difference (HSD) test to compare all pairs, as shown in Table 1. Regarding the modulus, Y orientation shows the highest modulus (0.96 Mpa) compared to the values for X and Z orientation (0.78 MPa and 0.87 MPa respectively). ANOVA shows a significant difference among the orientations with a p-value of 0.0371. From the Tukey test, the pair of X and Y orientations shows a significant difference. For the elongation, Z orientation shows the highest elongation (66.37%), while X and Y orientations show the lower values. (34.67% and 52.20% respectively). The pair of X and Z orientations shows a significant difference from Tukey test. The ultimate tensile strength is largest in the Z orientation (0.49 MPa) and smallest in the X orientation (0.23 MPa). ANOVA indicates a significant difference among the orientations with a p-value of 0.0024. The pairs of X-Y and X-Z orientations show a significant difference.

These differences are likely due to the interfacial quality between layers as a result of printing time. For example, in identical tensile specimens, X-orientation printing takes 72 layers and 39 min to complete, whereas Z orientation printing takes 2400 layers and 1490 min to complete. A longer printing time increases the chances of light exposure further strengthening the interface between layers, which usually creates weak spots due to under-curing. This explanation is supported by the benefits of over-curing in Z orientation and a poor level of curing between each pixel in DMD [26, 31]. They also described the modulus and ultimate strength as being the highest in the Z orientation. As a remark, printing orientations provide the part anisotropy.

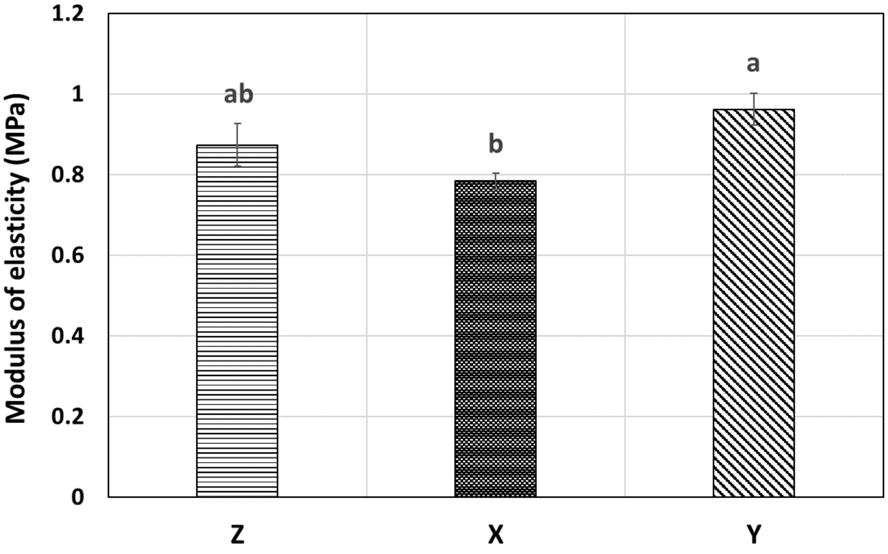

(a)

Figure 6. The results for mechanical properties (a) modulus of elasticity, (b) elongation, (c) Ultimate strength. Significant differences ($p < 0.05$) are indicated by the letters above the bar, determined by ANOVA and Tukey's tests. Orientations not connected by the same letter are significantly different.

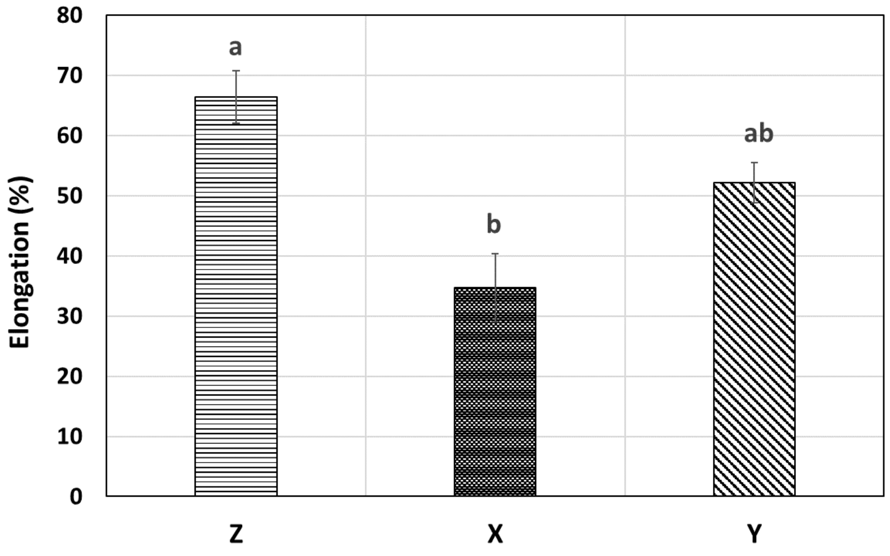

(b)

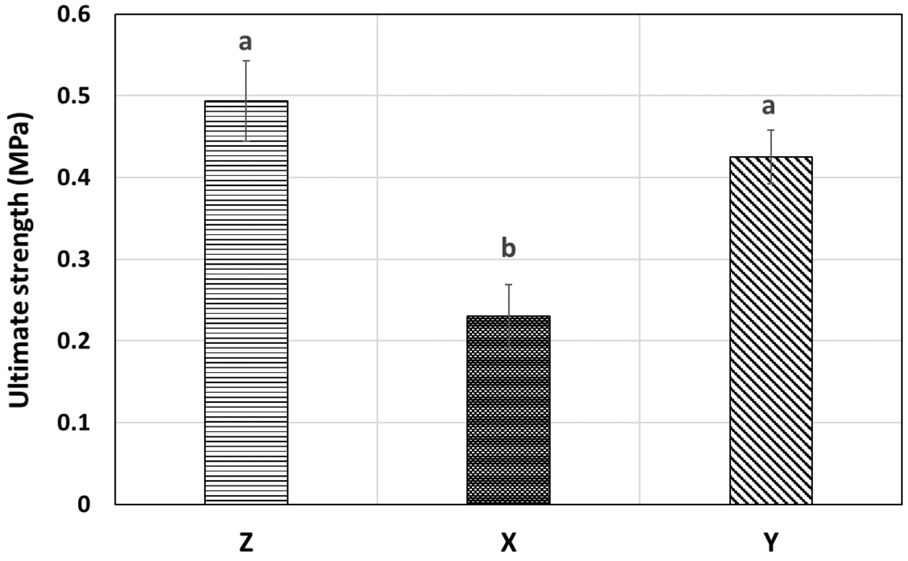

(c)

Figure 6 Continued.

Table 1 Statistical analysis with ANOVA and Tukey-Kramer HSD Test※

Modulus of Elasticity

Orientation	Mean	F	P-value
Z	0.87 ± 0.05^{ab}	4.1375	0.0371
X	0.78 ± 0.02^{b}		
Y	0.96 ± 0.04^{a}		

Elongation

Orientation	Mean	F	P-value
Z	66.37 ± 4.32^{a}	10.2479	0.0016
X	34.67 ± 5.63^{b}		
Y	52.21 ± 3.34^{ab}		

Ultimate Strength

Orientation	Mean	F	P-value
Z	0.49 ± 0.05^{a}	9.2910	0.0024
X	0.23 ± 0.04^{b}		
Y	0.42 ± 0.03^{a}		

※ **Significant differences ($p < 0.05$) are indicated by the letters above the mean, determined by ANOVA and Tukey's tests. Orientations not connected by the same letter are significantly different.**

2.4.3. Postcure Shrinkage

Figure 7 shows the results for postcure shrinkage with the different cube sizes and printing orientations. The error bars represent the standard error. The overall shrinkage rates fall between 0.15 % and 0.52 %. This range of shrinkage is small compared to that of commercial SLA or DLP resins, which range from 0.19% to 1.34 % [30]. One main reason for small shrinkage is that no solvent or additives are used in this PDMS. The evaporation of solvent and expansion/shrinkage of the additives could lead to significant volume change [29, 35]. Despite small shrinkage, it can be seen that the larger cubes shrink less than the smaller cubes. This is probably because larger cubes take more printing time and are more likely to be exposed to more light (from ambient or reflection) compared to smaller cubes. As a result, larger cubes have higher polymer conversion and are thus less sensitive to additional exposure at the post-process. Concerning the printing orientation, the Z-orientation shows the least shrinkage for all cubes, because it has a better level of curing through the layers. For the same reason, more exposure means a higher rate of conversion and less sensitivity to the additional UV exposure.

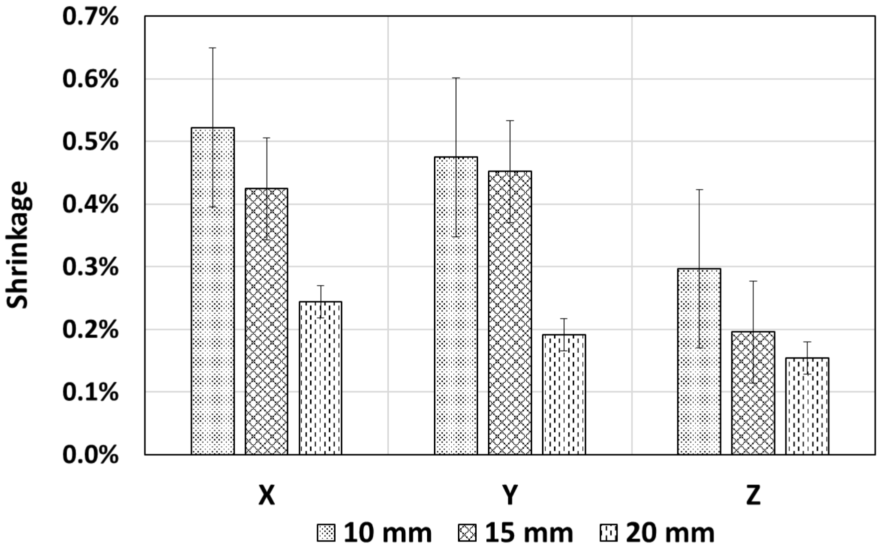

Figure 7. The results for postcure shrinkage with the different cube sizes of 10 mm, 15 mm, and 20 mm and printing orientations.

2.4.4. Separation Issue

Separation issue remains challenging in PDMS VP. Even though the DLP printer has a Teflon layer to reduce the separation force, some structures failed during printing. Separation force could make significant impacts on PDMS due to the low modulus and strength. Two solutions were used to overcome the separation issue, slow peeling speed and additional support structure. In this study, a peeling speed of 0.0625 mm/s was used as opposed to the default speed of 0.2500 mm/s. PDMS is a viscoelastic material, which tends to become stiffer and more brittle under high strain rates; therefore, slower speeds provide a lower strain rate to avoid large stress. In addition, large peeling speeds create a large shear force from the uncured resin which can tear down the printed structure during movement. Although creating additional supports is a solution, it introduces other practical issues including support removal process, additional material consumption, and printing time.

2.5. Conclusion

This study investigated a silicone 3D printing with DLP process. The UV-curable silicone photopolymer was prepared with an in-house methacrylated PDMS and commercial photoinitiator TPO-L. The printability of the silicone was demonstrated with a commercial DLP printer. Using the optimized printing parameters, good dimensional accuracies were achieved with an average error of 1.3%. The printed PDMS showed high directionality in the modulus, elongation, and strength due to the layering direction and printing time. Minimal postcure shrinkages were achieved with the average shrinkage rate of 0.3%. Despite a successful demonstration of PDMS printing, the separation issue in DLP remains challenging and requires further research and development to overcome.

3. FEASIBILITY STUDY OF SILICONE STEREOLITHOGRAPHY WITH AN OPTICALLY CREATED DEAD ZONE*

3.1. Abstract

This study* is about a feasibility study of an optically created dead zone for UV-curable silicone. The previous study observed that the silicone VP process has the separation issue which forms between the cured part and vat at each layer. Oxygen-inhibition is commonly adopted as a solution to make a dead zone between the vat bottom and the curing layer, but it is limited by the size, material, and environment. Herein, a method to optically create the dead zone by low one photon polymerization (LOPP) was investigated. LOPP is achieved by a low-absorbance wavelength and a gradient light beam. Two sets of the experiments, stationary exposure and moving exposure, were conducted with two low-absorbance wavelengths (375 nm and 385 nm) for a formulated UV-curable silicone. The first experiment measured the effect of beam power; the second experiment measured the effect of scanning speed. The results show that the lower-absorbance wavelength (385 nm) generates a larger, more stable dead zone and a smaller curing spot in both experiments, while the 375 nm wavelength produces a rapidly changed dead zone in the stationary condition and nearly no dead

---

*Reprinted with permission from "Feasibility study of silicone stereolithography with an optically created dead zone." Kim, D.S., Suriboot, J., Grunlan, M.A. and Tai, B.L., 2019, *Additive Manufacturing*, *29*, 100-793. Copyright 2019 by Elsevier B.V.

zone in the moving condition. The curing speed of 385 nm at the same power level was 10 times slower than 375 nm, but could be scaled up nonlinearly by the beam power. A tripled light power of 385 nm can accelerate the process by a factor of 7 and be comparable to that of 375 nm. Thus, this study confirms the feasibility of an optically created dead zone and also uncovers the necessity of high-power light source for this application.

3.2. Introduction

Silicones have a variety of applications in many sectors because of their unique properties, including elasticity and biocompatibility as well as corrosion and temperature resistance. Conventional methods for fabricating silicone are molding or soft lithography [17, 18] but these methods are limited for complex designs involving optimized topology or internal structures [19, 20]. The emergence of additive manufacturing offers an alternative means of fabrication of such structures for various polymers but is less useful for silicones due to their low modulus. For instance, while commercial 3D printers can produce silicone structures, these cannot achieve complex features. Thus, there remains a need for developing techniques to 3D print silicones with complex structures for broad applications in medical simulators, tissue engineering structures, soft robotics, microfluidic devices, and many others [2, 3, 36, 37].

Recent studies have evaluated extrusion-based 3D printing of silicones having different cure chemistries. Thermal-curable silicones are widely available and can be incorporated into an extrusion-based process [21, 22]. This process is simple, requiring only an extruder, pressurizing pump, printing platform, controller, and a heater. However, heat also causes issues with clogging and geometrical inaccuracy. Alternatively, Plott et al. demonstrated an extrusion-based process with a moisture-curable silicone [8]. They investigated part deformation and voids that may compromise structural strength and geometrical accuracy. Muthusamy et al. reported inclusion of a support material for a moisture-curable silicone to produce overhanging structures [23]. Porter et al. presented an extrusion-based process with an ultraviolet (UV)-curable silicone [38]. They added a carbon black to the resin to minimize electrostatic repulsion, in-nozzle curing, and extrudate slumping.

In all extrusion-based methods for 3D printing of silicones, a rough finish and an interfacial boundary are inevitable. Thus, vat photopolymerization, by utilizing an immersed photo-curing process, has been explored for a better outcome. For example, Au et al. reported stereolithography (SLA) with an UV-curable silicone for the preparation of microfluidic devices [9]. Bhattacharjee et al. developed an UV-curable silicone for digital light processing (DLP) that matches the properties of the commercial PDMS Sylgard-184 [10]. However, their silicone takes longer time (several seconds) to cure than commercial acrylate photopolymers used in DLP/SLA. In addition to the material itself, another major obstacle to SLA and DLP of silicones and other polymers is separation [11-13], arising from the adhesion between a cured polymer and the bottom surface of a vat that has a significant bonding force [6]. To solve the separation issue, researchers have investigated various methods, including a non-stick coating in the interface, detaching motions, ultrasonic vibration, and chemical inhibition phenomena.

Commonly, a Teflon sheet (or silicone for non-silicone resins) is used at the bottom of a vat as a non-stick layer and a detaching motion is applied after each layer of print to separate the cured part from the vat [6, 13, 14]. However, the non-stick sheet needs to be replaced regularly, and the detaching motion increases the total printing time. Alternatively, Jin et al. applied ultrasonic vibrations to the interface to aid the separation [39], but the vibrations resulted in a poor surface finish. Tumbleston et al. demonstrated a DLP process with oxygen inhibition phenomenon [15]. An oxygen-permeable window was installed at the bottom of a vat. Oxygen gas molecules are able to diffuse through the window, creating a “dead zone” at the interface of the vat and a cured part. Although the oxygen-induced dead zone can effectively eliminate the separation problem and speed up the printing time, it is only applicable (and sensitive) to specific photopolymers with free radical polymerization. Further, gas diffusion often results in a non-uniform thickness of the dead zone, which makes it difficult to print a solid and flat surface [16]. The limited manufacturable size of the permeable window is another constraint of this approach.

Herein, we investigated the feasibility an optically created dead zone using low one photon polymerization (LOPP) for the vat photopolymerization of silicone. LOPP is a low absorbance polymerization process as opposed to common one-photon polymerization (OPP) with high absorbance [40, 41]. In the context of vat photopolymerization, LOPP can be achieved by a gradient light beam and a low-absorbance wavelength, which together can penetrate into the liquid resin and cure the polymer only around the focusing spot as shown in Figure 8. The uncured region near the resin surface is considered the optically created dead zone. LOPP-based 3D printing idea has been explored by the authors' prior studies for an in-liquid 3D curing scheme [42, 43]. However, it was found that the LOPP outcome is sensitive to the selected wavelength despite within a low-absorbance region. Also, polymerization takes a long time (minutes) to initiate but a short time (few seconds) to grow and complete, meaning that the optically created dead zone can vanish quickly. In this case, the printing process can be time-consuming as well as unstable because the dead zone varies over time. To fully understand the dead zone behavior, a factorial design of experiment was conducted herein to quantitatively measure the effects of wavelength, light power, and scanning speed on the printing time and dimensions to better assess the feasibility of this process. All experiments were performed on a custom-built motion system with a UV light source and necessary optical components. Further, to minimize other extraneous variables for a controlled experiment, a custom UV-curable silicone was prepared wherein the levels of photoinitiator and an oxygen scavenger could be controlled. This is essential because commercial UV-curable silicones are sensitive to oxygen and will produce coupled-effects with oxygen inhibition which would influence the factorial experiment. Commercial photopolymers also do not have the desired absorbance spectrum (i.e., a low-absorbance UV wavelength).

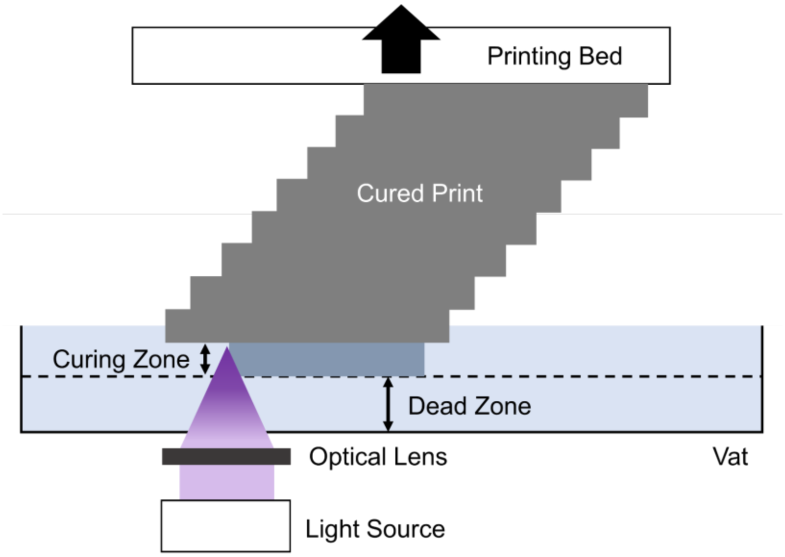

Figure 8. A conceptual drawing of the proposed printing process with an optically created dead zone.

3.3. Material and Methods

3.3.1. Silicone Material Preparation

UV-curable silicone, a methacrylated polydimethylsiloxane (PDMS)-macromer, was synthesized via triflic acid-catalyzed ring-opening polymerization of D_4 and methacrylate endcapping agent. To a 500 mL round bottom flask equipped with a magnetic stir bar, D_4 (200g, 674.28 mmol), 1,3-bis(3-methacryloxypropyl) tetramethyldisiloxane (16.30 g, 42 mmol), and triflic acid (320 µL) were added. The mixture was allowed to stir at room temperature for 12 h. The reaction was quenched by adding HMDS (752 µL) and allowed to stir for 1 h. The resulting mixture was filtered through filter paper and subsequently dried under vacuum to yield a clear colorless oil

(210 g, 97%). Figure 9 shows the chemical structure of the synthesized PDMS-macromer based on nuclear magnetic resonance spectroscopy (NMR) Varian Inova 500 MHz (Palo Alto, CA, USA).

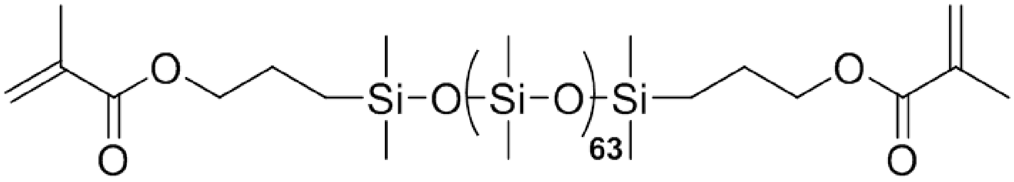

Figure 9. The chemical structure of the synthesized PDMS-macromer

Table 2 shows the data of the PDMS-macromer from a gel permeation chromatography (GPC) Viscotek 270 detector (Malvern Panalytical, MA, USA), a rheometer Physica MCR 301 (Anton Paar, Graz, Austria), a DSC Q100 (TA Instruments, DE, USA), and a TGA Q50 (TA Instruments, DE, USA). The polydispersity index (PDI) of 1.86 is the ratio of weight average molecular weight (Mw) to number average molecular weight (Mn), which describes the broadness of a molecular weight distribution. The numbers less than 2 is generally acceptable. Glass transition temperature (Tg) and Thermogravimetric Analysis (TGA) indicate the upper and lower limits of the operating range of the material.

Table 2 Material data of the synthesized PDMS-macromer

	Mw	**Mn**	**PDI**	**Viscosity**	**T_g**	**TGA**
PDMS-macromer	10400	5600	1.86	109 cP	-124°C	418°C

2-Hydroxy-2-methylpropiophenone (2H2M) was used as a photoinitiator (Sigma-Aldrich, MO, USA) for this PDMS system. Figure 10 shows the absorbance spectrum of the photoinitiator measured by a U-4100 spectrophotometer (Hitachi, Tokyo, Japan). The absorbance rates decrease to below 0.1 after 350 nm wavelength. To realize the LOPP effect, two wavelengths were selected based on the absorbance rates and the availability of the light sources. The first wavelength selected was 375 nm with an absorbance rate of 0.011. The second wavelength selected was 385 nm with an absorbance rate of 0.001.

To minimize the effect of oxygen inhibition from exposure to the ambient air, 0.1 wt.% N-vinyl pyrrolidone (NVP) was added to the PDMS resin. NVP is commonly known as an oxygen scavenger that improves the curing of acrylate-based monomers or macromers in the air. Researchers have reported that NVP gives higher double bond conversion of acrylates, and copolymerizes with acrylates and becomes part of the cured matrix; thus, there are no by-products or impurities generated from NVP in the cured materials [44, 45]. After mixing, the resin was degassed for 15 minutes in a vacuum chamber to minimize the oxygen content.

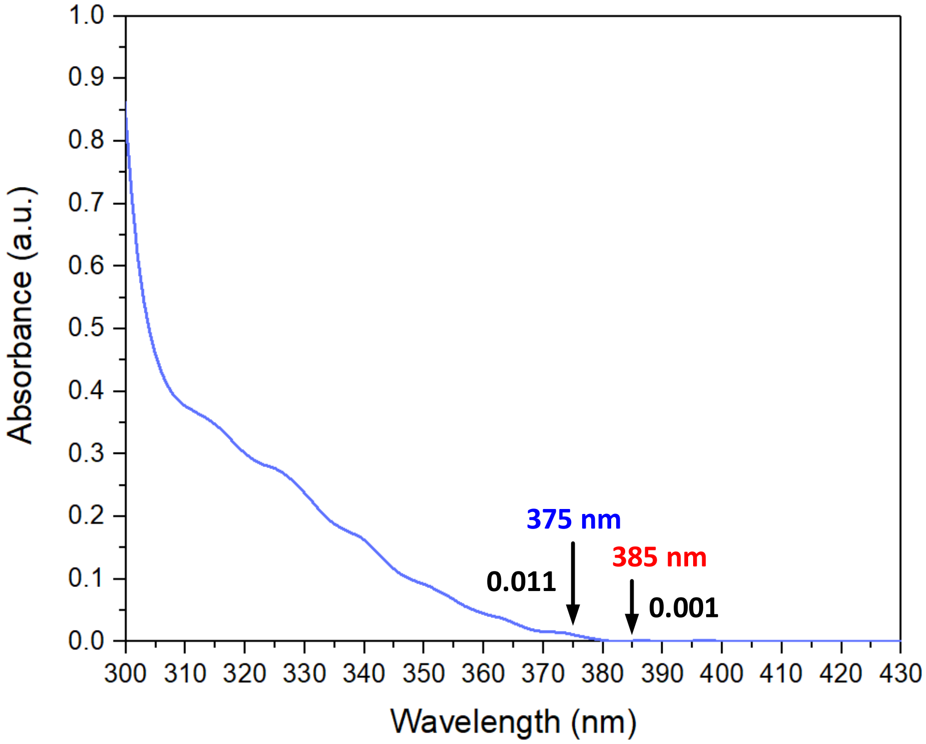

Figure 10. Measured absorbance spectrum of the photoinitiator.

3.3.2. Experimental Setup

Figure 11 shows the experimental setup. A LED light unit was used as the light source and controlled by an Arduino control board with a millisecond timer. Two different wavelengths of LEDs, 375 nm and 385 nm, were obtained from the same manufacturer (Advanced Illumination, Rochester, VT). A series of optical lenses were used to condition the light, consisting of a collimating lens, a bandpass filter, a convex lens, a concave lens, and a focusing lens (Edmund Optics, Barrington, NJ). The collimating lens converts the LED light into a uniform and parallel light beam. The bandpass filter allows a specific wavelength to exit from the incoming light beam. This step is needed because the beam spectrum of an LED is not as sharp at the specified wavelength as a laser. Then, a convex lens and a concave lens together can adjust the beam diameter from the bandpass filter to match with the diameter of the focusing lens, thereby minimizing the loss of beam power. The final lens focuses the beam with the effective focal length (EFL) of 13.0 mm and a numerical aperture of 1 to produce the largest beam gradient in air. On the build platform, a small acrylic box with the external dimensions of 25.4 mm by 25.4 mm by 6.3 mm was used as a resin vat. The vat and optics were attached on a three-axis motion stage controlled by G-codes with a resolution 2.5 μm (Moog Animatics, Milpitas, CA). To ensure the quality of the produced light beam, the beam after the focusing lens was characterized with a beam profiler (Edmund Optics, Barrington, NJ) and a power meter (Thorlab, Newton, NJ). The beam profile showed a Gaussian distribution (92.55% fitness) with a diameter of 1.1 mm defined by the width at $1/e^2$ of the peak intensity. The 375 nm LED had a maximum power of 3.6 mW, and the 385 nm LED had 11.3 mW. The difference was caused by the different transmission efficiencies of the bandpass filters used. To adjust the beam power (between zero and the maximum) for the design of experiment, different neutral density filters were used instead of the PWM module in Arduino to avoid power fluctuation.

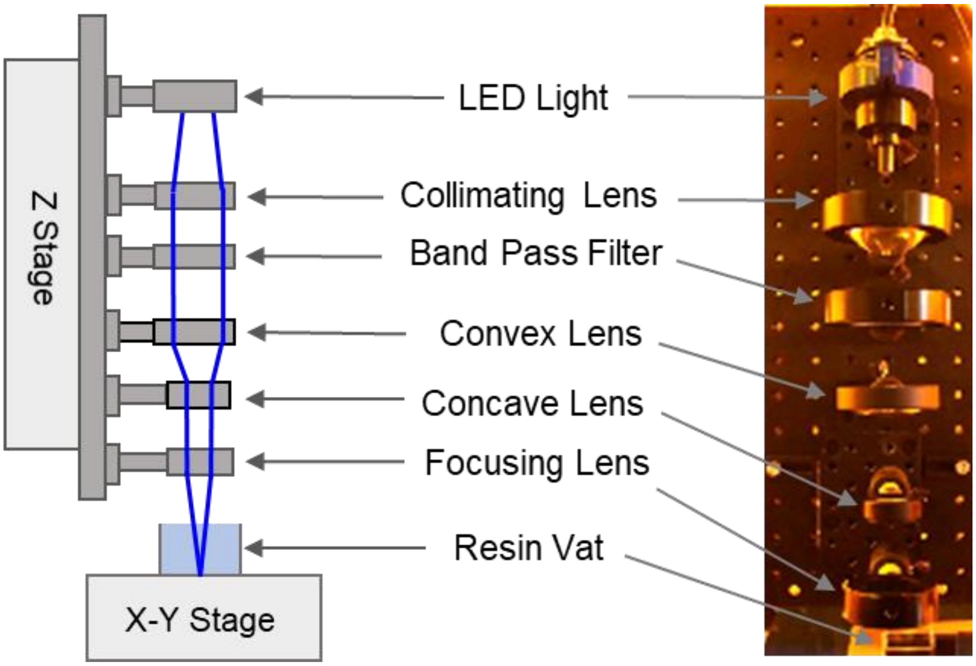

Figure 11. Details for the optical lens array of the experimental testbed.

3.3.3. Design of Experiment

Two set of experiments were conducted with two different exposure conditions: stationary exposure and moving exposure. The former was to observe the dead zone as a function of exposure time, and the later was to observe the dead zone as a function of scanning speed.

For the stationary exposure condition, a two-variable (wavelength and power) factorial design of experiment was conducted as shown in Table 3. The actual powers were slightly different from the planned power levels due to the neutral density filters used. Two cases were noted “NA” in the table because the 2 mW of 385 nm could not cure anything for at least 3000 s and the 10 mW of 375 nm was beyond the physical limitation of the current setup. The dependent variables are the initiation time and the growth rate to characterize the polymerization process. The initiation time means the time needed to begin the curing, which reflects the potential printing speed. The growth rate measures how fast the cured spot expands over time, which reflects the stability of the dead zone. Figure 12 shows the testing method schematically. The resin container was filled with the silicone liquid resin, and the focal point of the beam was set at the bottom of the vat. The polymerization would begin at the vat bottom and form “pillars” toward the resin surface over time. For every given wavelength and power, the pillar size was measured at different exposure times (i.e., one data point for every time interval) until it reached the vat depth. The results would reveal the easiness to generate and control the dead zone. To measure the pillar height, the liquid resin needed to be drained to catch the cured parts with a sieve because both the resin and cure parts are transparent. The height of each cured spot was measured by a microscope with 0.01 mm resolution (Dino-Lite, Torrance, CA). It should be noted that small cured spots less than 1 mm could hardly be caught by the sieve. The experiment was repeated three time for each case noted in Table 3.

Table 3 A fractional factorial design for the stationary exposure test

Planned power	Actual power for 375 nm	Actual power for 385 nm
2 mW	2.3 mW	NA
4 mW	3.6 mW	3.4 mW
10 mW	NA	11.3 mW

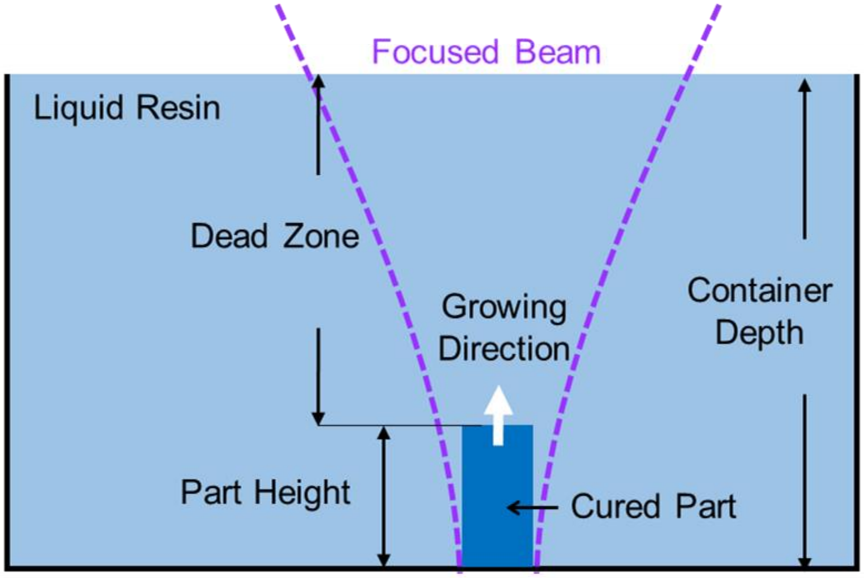

Figure 12. Schematic of the stationary exposure test.

For the second set of experiments with a moving exposure condition, each wavelength was tested individually to see the effect of the scanning speed as shown in Figure 13. The testing parameters are shown in Table 4, where the maximum power of each wavelength is used. Five different scanning speeds were selected for each wavelength between no curing and over-curing. In this experiment, the resin container was filled with the silicone liquid resin, and the beam was focused at the bottom of the container moving from left to right. The dependent variables are the width, length, and height of the print measured by a microscope. Similar to the first experiment, the structure was obtained after the resin is drained. The part dimensions indicate the current printing accuracy and resolution; the height difference from the vat surface indicates the dead zone depth.

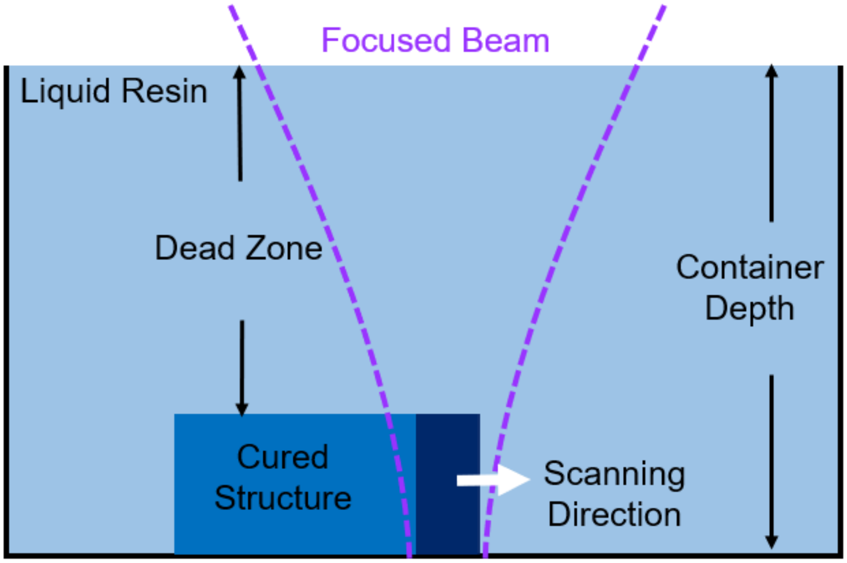

Figure 13. Schematic of the moving exposure test.

Table 4 Parameters for the moving exposure test

Wavelength	**375 nm**	**385 nm**
Maximum beam power	**3.6 mW**	**11.3 mW**
Scanning speed (mm/min)	0.60, 0.96, 1.20, 1.60, 2.40	0.60, 0.96, 1.07, 1.20, 1.60

3.4. Results

3.4.1. Stationary Exposure Test

3.4.1.1. 375 nm Wavelength

Figure 14 shows the images of actual samples at different exposure times with beam powers of 2.3 mW and 3.6 mW. The cured parts were ovoid in shape. With a higher beam power (3.6 mW), the shape of the parts became more cylindrical than the one with a lower beam power. Figure 15 shows the measured height change over time. Error bars represent one standard deviation from measured data. For the beam power of 2.3 mW, the exposure time was tested from 136 s to 144 s with a 1 s interval. No curing was found until 138 s. The first observable cured part was at 139 s with a height of 1.26 mm. This indicates the largest observable dead zone about 3.74 mm considering the vat depth of 5.0 mm. At 144 s, the pillar had reached the container depth of 5.0 mm. Between 139 seconds and 144 seconds, the linear fitted trend line represents a vertical growth rate of the pillar, which is about 0.74 mm/s.

For the results of 3.6 mW, the appearance of the first pillar was shortened to 120 s, which is equivalent to a total exposure of 432 mJ, compared to 319.7 mJ of the 2.3 mW case. The first observable pillar was 2.26 mm in height, which corresponded to a dead zone of 2.74 mm. At 123 s, the pillar had reached the container depth of 5.0 mm. The vertical growth rate increased to 0.91 mm/s, about 20% faster than that of the 2.3 mW case. The power shows a proportional effect on both the initiation time and growth rate.

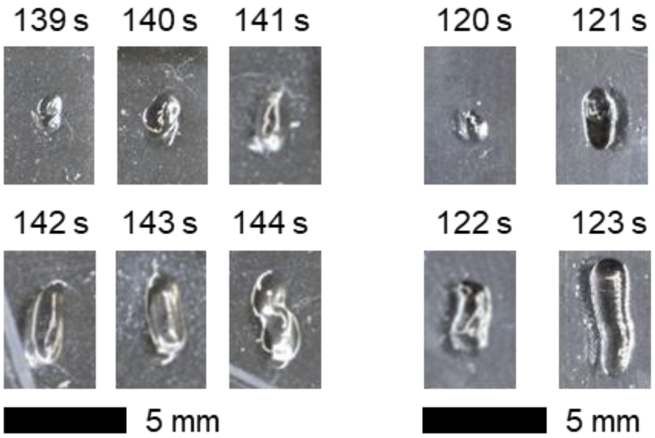

(a) (b)

Figure 14. Physical samples from the stationary exposure tests: (a) with 375 nm wavelength and 2.3 mW of beam power (exposure time: 139 s ~ 144 s), (b) with 375nm wavelength and 3.6 mW of beam power (exposure time: 120 s ~ 123 s).

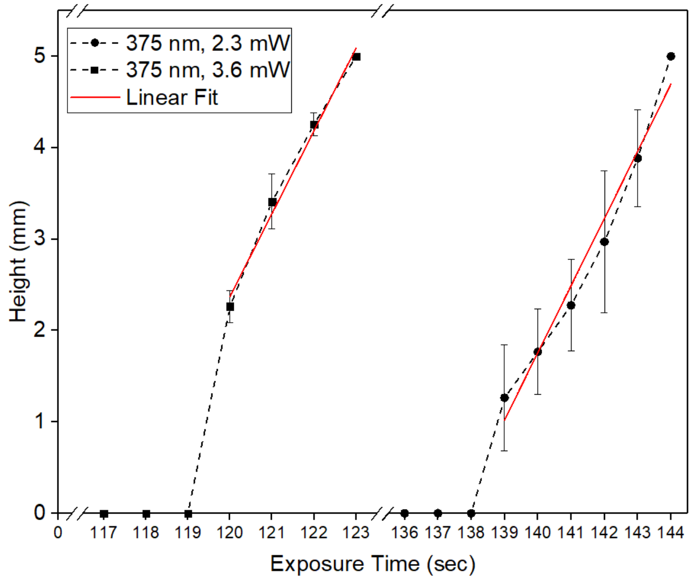

Figure 15. Results of the stationary exposure test with 375 nm wavelength and 2.3 mW and 3.6 mW of beam power. The error bars represent one standard deviation of the measured heights.

3.4.1.2. 385 nm Wavelength

Figure 16 shows the images of actual samples with 385 nm wavelength and beam powers of 3.4 mW and 11.3 mW, respectively. The shape of cured parts was conical with a sharp tip pointing upward. Unlike the 375 nm cases, these cured parts had a very well-defined contour. With a lower beam power (3.4 mW), the tips of the parts were much sharper than the ones with the higher power. The differences in shape are caused by the irradiance distribution around the focusing spot, which be further discussed in a later section.

Figure 17 shows the measured heights for 3.4 mW and 11.3 mW powers. Error bars represent one standard deviation from measured data. For the beam power of 3.4 mW, the exposure time testing was extended from 300 s to 2400 s with 300 s interval due to the slow curing process. No curing was observed until 1200 s. The first pillar was found with a height of 1.35 mm, which corresponded to a dead zone of 3.65 mm. The growth is expected to continue over 2400 s but was not tested due to an extreme time needed. Between 1500 seconds and 2400 seconds, the data showed a significantly slower vertical growth rate around 0.0015 mm/s.

For the beam power of 11.3 mW, the exposure time was tested from 145 s to 185 s with a 5 s interval. The initiation time was shortened to 165 s. The first pillar had a height of 1.46 mm, which corresponded to a dead zone of 3.54 mm. Between 170 seconds and 185 seconds, the vertical growth rate was 0.095 mm/s. Compared to the data of 3.4 mW, the results of 11.3 mW show a substantial increase in both initiation time and growth rate.

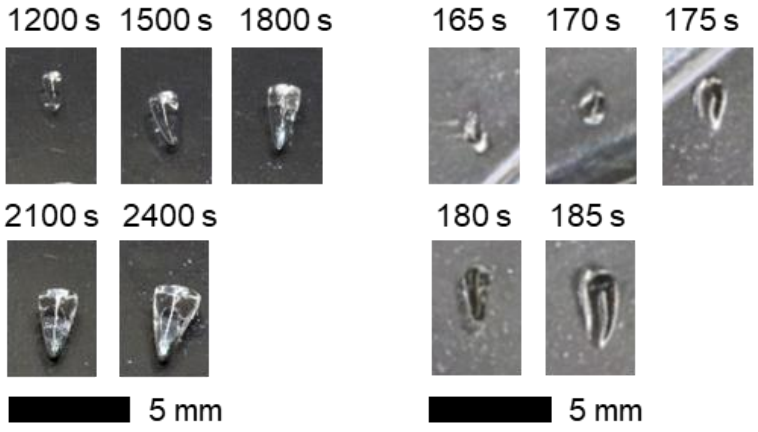

(a) (b)

Figure 16. Physical samples from the stationary exposure tests: (a) with 385 nm wavelength and 3.4 mW of beam power (exposure time: 1200 s ~ 2400 s) and (b) with 385 nm wavelength and 11.3 mW of beam power (exposure time: 165 s ~185 s).

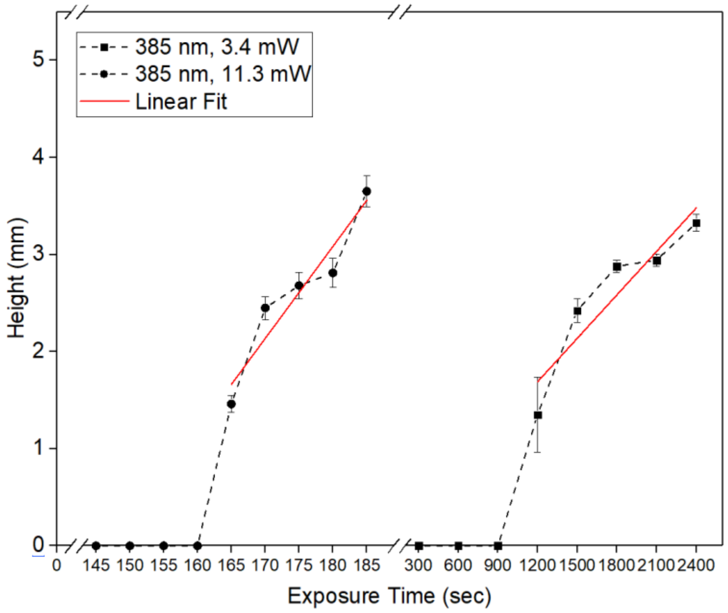

Figure 17. Results of the stationary exposure test with 385 nm wavelength and 3.4 mW and 11.3 mW of beam powers. The error bars represent one standard deviation of the measured heights.

Table 5 summarizes the results of the inhibition time and growth rate in the stationary exposure test with 375 nm and 385 nm wavelengths. Note the differences are all statistically distinguishable. It can be seen that the initiation time of 385 nm was 10 times longer than that of 375 nm, which coincides with the absorbance spectrum in Figure 10. The growth rate, on the other hand, is about 600 times slower. The growth rate also indicates the reduction rate of the dead zone. A slower growth rate is desired because it is easier to control the dead zone size, but the 1200 s initiation time is not practical. By scaling the light power by 3 times for the 385 nm case, the initiation time was increased by 7 times and the growth rate is increased by 60 times, showing a highly non-linear scaling effect. However, the growth rate of 0.095 mm/s is still considered slow. The results suggested that low absorbance wavelength with high power is preferred for LOPP-based printing. The printing speed can be scaled non-linearly with the light power, unlike conventional vat photopolymerization processes.

Table 5 Initiation time and growth rate from the stationary exposure test

Wavelength	**375 nm**		**385 nm**	
Beam power	**2.3 mW**	**3.6 mW**	**3.4 mW**	**11.3 mW**
Initiation time (s)	139	120	1200	165
Growth rate (mm/s)	0.74	0.91	0.0015	0.095

3.4.2. Moving Exposure Test

3.4.2.1. 375 nm Wavelength

Figure 18 shows the actual samples with 375 nm wavelength and beam power of 3.6 mW. The scanning distance was set at 10 mm from left to right. The slowest scanning speed (0.60 mm/min) and the fastest one (2.40 mm/min) were excluded from the data set due to over-curing and non-curing conditions, respectively. As seen, the cured parts had a wall-shape structure with upright position. The parts mostly showed a uniform length, height, and width. To quantify the shape variation, five measurements at different sections of each sample were taken in length, height, and width. The sectioning details are shown in Figure 19 under a digital microscope and the data is plotted in Figure 20 with a box chart.

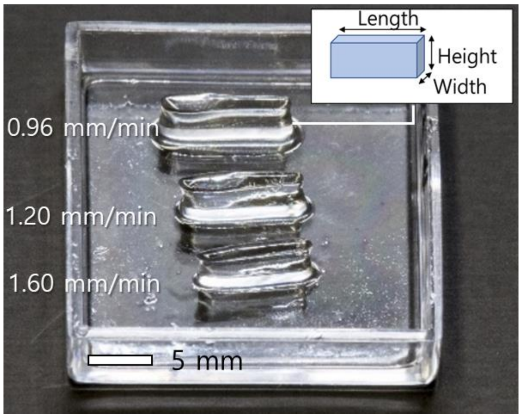

Figure 18. Physical samples from the moving exposure tests with 375 nm wavelength and 3.6 mW of beam power at 0.96 mm/min, 1.20 mm/min, and 1.60 mm/min of scanning speeds.

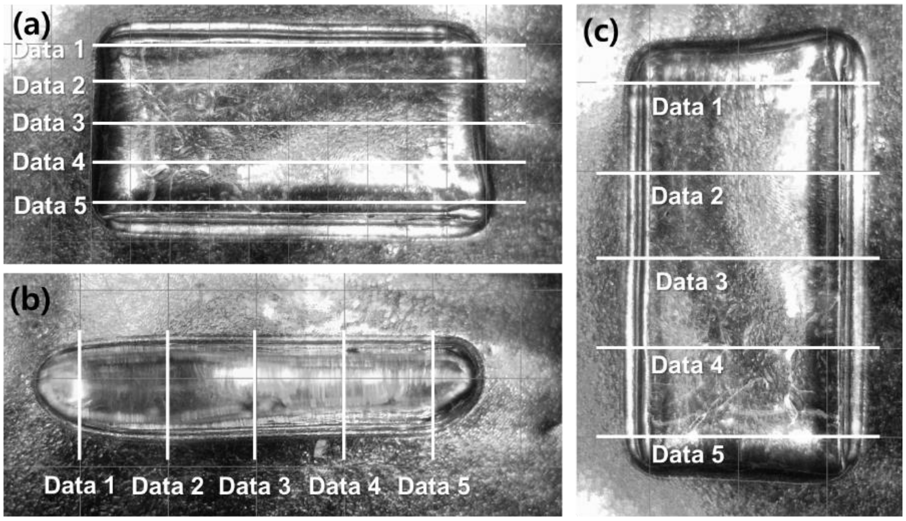

Figure 19. Dimensional measurements for the physical sample with 0.96 mm/min of scanning speed and 375 nm wavelength in the moving exposure tests (a) length (b) width (c) height.

As shown in the plot, the widths are all similar (1.0, 1.14, and 0.98 mm, respectively), which coincide with the beam diameter at the focusing spot (1.1 mm). The length of the structures decreases (away from nominal 10 mm length) when the scanning speed increases. No curing occurs at the beginning for faster feed rates. The heights are also similar (4.62, 4.56, and 4.53 mm, respectively) but all are close to the 5 mm vat depth. This indicates nearly no dead zone and high layer thickness, which are both undesired in a real printing application. In conclusion, 375 nm wavelength can produce consistent dimensions but is unable to create a clear dead.

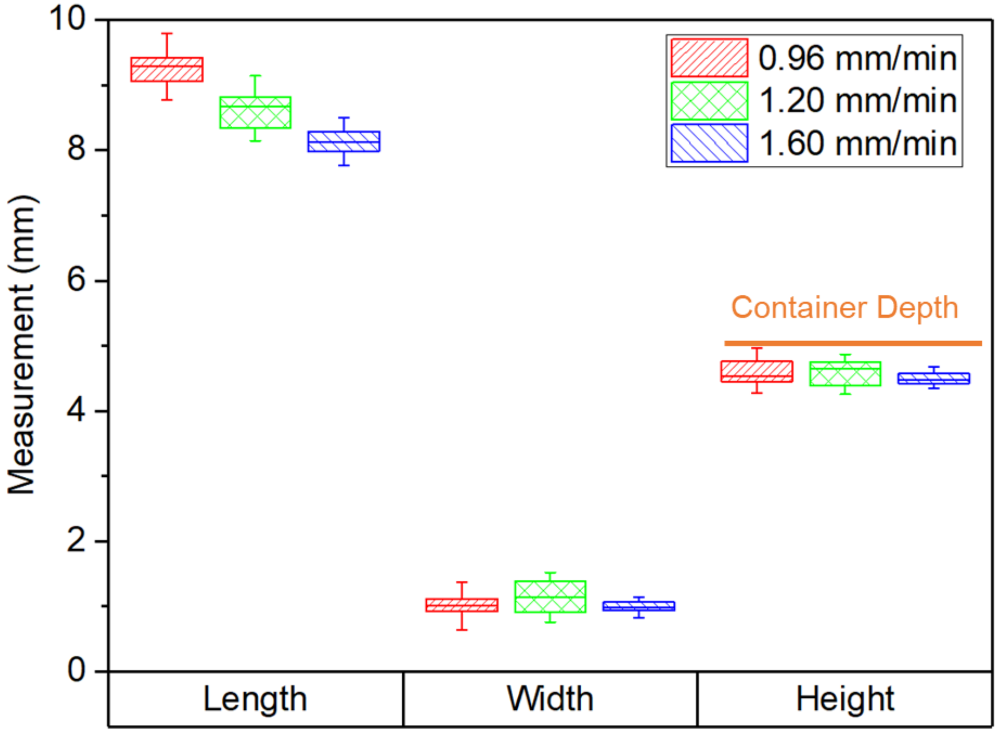

Figure 20. Results of the moving exposure test with 375 nm wavelength and 0.96 mm/min, 1.20 mm/min, and 1.60 mm/min of scanning speeds.

3.4.2.2. 385 nm Wavelength

Figure 21 shows the actual samples with 385 nm wavelength and beam power of 11.3 mW. The scanning distance was set at 20 mm from left to right. Note the parts in the image have fallen to the side. Variations in height can be clearly seen in these structures as compared to those of 375 nm. Using the same measurement procedure, Figure 22 represents the dimension results of the moving exposure test with 385 nm wavelength and beam power of 11.3 mW. The slowest scanning speed (0.60 mm/min) was not shown because of over curing. The fastest speed (1.60 mm/min) was also excluded due to no curing. As seen, the length of the structures decreases only slightly as the scanning speed increases, unlike the 375 nm case. The widths are about 0.68 mm on average. The heights are significantly lower than the depth of the vat, indicating a noticeable dead zone of at least 2.5 mm. However, the heights also show a wide distribution within a structure in particular for a low scanning speed (0.96 mm/min). The heights for 1.07 mm/min and 1.20 mm/min are more consistent. Further, the wall structures tend to be thinner at the top and wider at the bottom, which correspond to the conical shape in the stationary exposure test. In conclusion, 385 nm wavelength produces a very clear dead zone but more variation in depth, which requires a more delicate process control in printing.

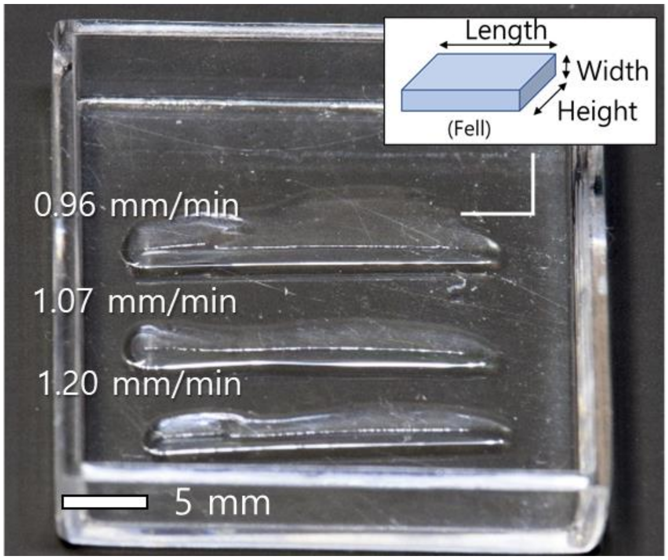

Figure 21. Physical samples from the moving exposure tests with 385 nm wavelength and 11.3 mW of beam power at 0.96 mm/min, 1.07 mm/min, and 1.20 mm/min of scanning speeds.

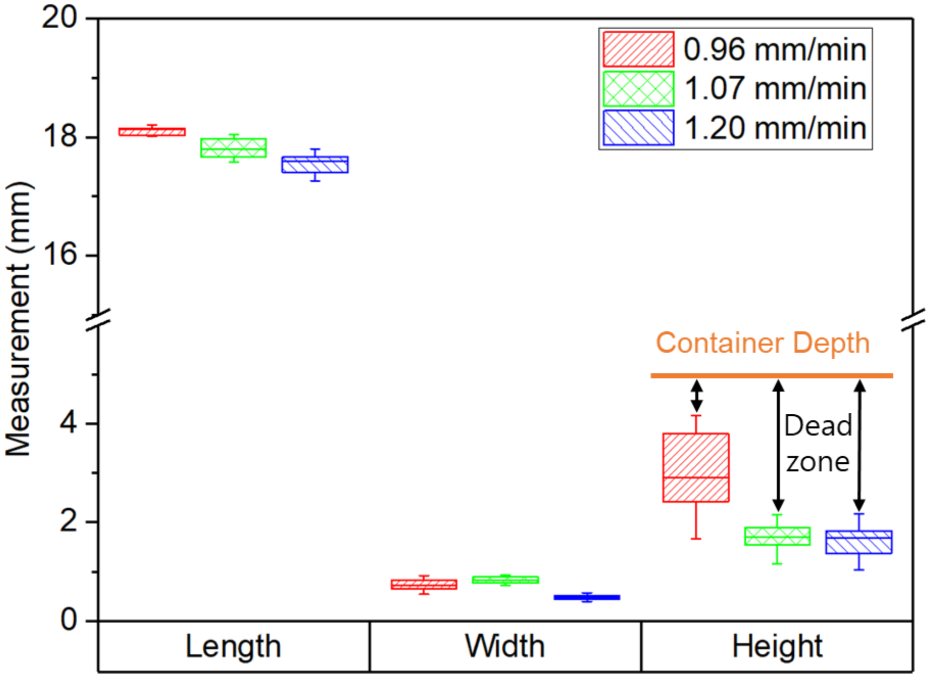

Figure 22. Results of the moving exposure test with 385 nm wavelength and 0.96 mm/min, 1.07 mm/min, and 1.20 mm/min of scanning speeds.

3.5. Discussion

The optically created dead zone can be successfully produced by LOPP, but the results are significantly different between the wavelengths. The 375 nm and 385 nm show the polymerization at different initiation times and growth rates due to their different absorbance rates. However, despite an identical light distribution (from the same optics), the 375 nm wavelength produces a more cylindrical shape while 385 nm produces a conical shape. Such a difference is likely caused by different growth rates and sensitivities to the light intensity. Despite a high power, the 385 nm wavelength has a very slow growth rate, which means that the polymerization would follow the beam intensity distribution tightly. Figure 23 (a) is a 2D numerically computed exposure distribution in an arbitrary unit (a. u.) for this particular gradient beam without considering light attenuation. As seen, the center line always has a higher exposure (and intensity) which drives a faster growth to form a triangular shape. In comparison, with a higher absorbance of 375 nm wavelength, the part tends to grow in all directions equally but confined by the beam boundary. Thus, an oval shape is formed. This indicates that wavelength results in fundamental difference in shape forming regardless of the beam power.

In the moving exposure test, a similar difference in shape can also be observed between the two wavelengths. The cross-section of the 385 nm produced structure is more triangular with a wider bottom and narrower top, while that of the 375 nm is nearly rectangular. Also, a faster scanning speed of 375 nm results in a shorter structure, but this phenomenon is not obvious in the 385 nm case. This is because the fast growth rate of 375 nm causes a rapid change of dead zone. Figure 23 (b) shows a 2D exposure map after a line scanning. As seen, the exposure is less at the beginning and the end of light scanning, and thus the curing in these regions may be incomplete under a quick scanning speed. For the wavelength with a high growth rate, the structure can form immediately when the exposure increases to a plateau toward the moving direction, as shown by the constant exposure region in the figure. As a result, the lengths can be shorter by up to one diameter of the beam size (about 1.1 mm in this study).

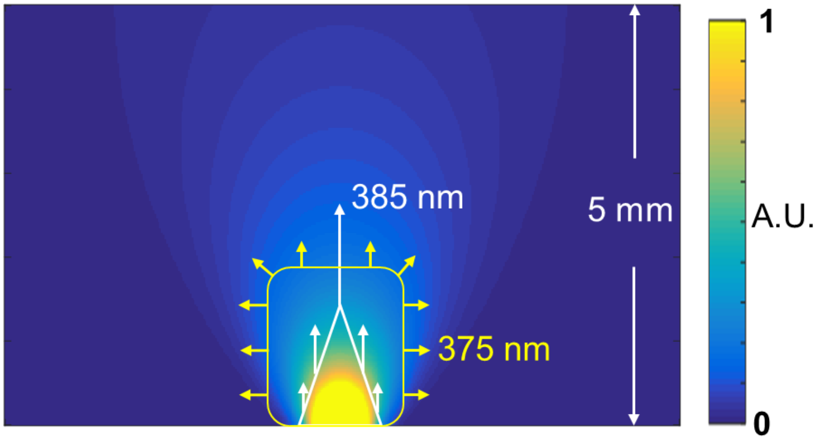

(a)

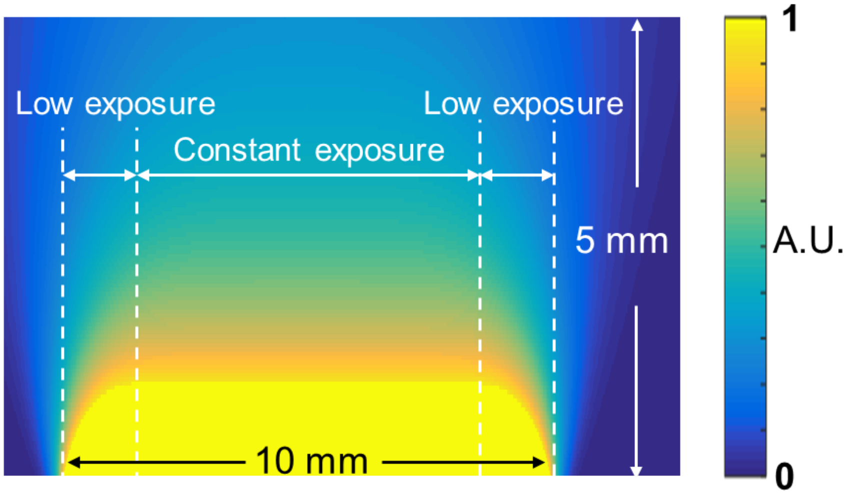

(b)

Figure 23. Numerically computed exposure distributions: (a) the stationary exposure condition and (b) the moving exposure condition.

By looking at the results within in the same wavelength, the beam power appears to have a highly non-linear scaling effect, unlike the commonly used Jacob’s model [28]. For example, in the 385 nm case, the 11.3 mW power speeds up the initiation time by 7 times and the growth rate by 60 times compared to 3.6 mW power. This is mainly due to the low-absorbance polymerization of LOPP. With the low-absorbance, the polymerization process has a long unsteady-state before reaching a steady-state. Polymerization involves reaction-diffusion kinetics including generation and consumption of free radicals and conversion rate of the material [46, 47]. A high absorbance wavelength can generate a sufficient amount of free radicals to be consumed despite a small beam power. The process would reach the steady-state when the free radical initiation rate is equivalent to the polymer termination rate. On the other hand, when a low-absorbance wavelength is used, the production of free radicals is slow and hardly be enough to reach a steady-state process. Thus, the process is highly dependent on the beam power. The abundant free radicals generated from a high beam power accelerate the initiation of the polymerization, thus speeding up the process non-linearly. Certainly, this is also related to the efficiency of a photoinitiator for the generation of the free radicals, consumption of the radicals by the material system, and properties of the photopolymer including a molecular weight and viscosity. That said, despite an equivalent energy absorption in both wavelengths, the polymerization behaviors will still be different.

Furthermore, it is found that the curing speed is faster in the moving exposure test than that in the stationary moving test when comparing a converted scanning speed from the initiation time and the beam diameter (1.1 mm). The equivalent scanning speeds from the stationary exposure test are 0.55 mm/min for 375 nm wavelength and

0.4 mm/min for 385 nm wavelength, which are at least twice faster. This is likely due to a pre-exposure effect on the resin by the diffracted beam from the multiple lens array. The optical aberration and diffraction cause the additional exposing area beside the focusing spot. The long experiment time in a scanning process causes additional exposure to the entire resin. This issue may be minimized by a shorter experiment time with a higher beam power and a narrow and well-defined beam focusing spot.

3.6. Conclusion

This study investigated silicone 3D printing with an optically created dead zone. Both results of 375 nm and 385 nm wavelength showed that a dead zone was produced through the LOPP effect, while different wavelengths resulted in drastically different initiation times, growth rates, and resulting cured shapes. The 375 nm wavelength presented a shorter initiation time, a faster growth rate, and a larger shape, indicating a faster printing but worse resolution. The dead zone was also not that obvious. On the other hand, the 385 nm wavelength produced a fine resolution and a large, stable dead zone due to a slower growth rate. However, the initiation time for 385 nm is much longer. Depending on the requirements of printing speed and resolution, different wavelengths can be selected for this technology.

Due to the relatively low power light source used herein (11.3 mW), slow polymerization/curing resulted (several minutes). Unlike conventional SLA or DLP using a light source in mW, a much higher power should be used for the LOPP enabled printing. Therefore, the future work will be focused on a high-power LOPP to analyze the scalability the process. Also, because of LOPP, the process is a low-absorbance polymerization and exhibits a highly non-linearity to the beam power. The nonlinear behavior may be beneficial to confining the curing volume on the focusing spot as well as to accelerating the printing speed.

4. CHARACTERIZATION OF ULTRA-LOW ABSORBANCE WAVELENGTH FOR CREATING OPTICAL DEAD ZONE

4.1. Abstract

The adhesion issue in vat photopolymerization has been a major challenge. Current solution with the dead zone created by oxygen inhibition is narrow and often uneven. Therefore, an alternative approach using the optically created dead zone was proposed in a prior study by means of low-absorbance wavelength and gradient beam. This study further investigates the use of ultra-low absorbance wavelength (405 nm) for the customized PDMS and compares the results to the published data for 375 nm and 385 nm in terms of the easiness to control the dead zone, geometry consistency, and printing time. Stationary and moving exposure conditions were tested with various exposure times and scanning speeds to observe the cure size. In results, the 405 nm produced a large and stable dead zone more than 4 mm (out of the 5 mm vat depth) with a range of time (up to 400 s) and speeds (0.21-0.28 mm/min). The 405 nm also shows a low geometrical variation (standard deviation less than 0.03 mm) for all the moving tests. However, 405 nm requires extremely high irradiance to offset the time loss from its ultra-low absorbance. The further analysis also shows that the time cannot be simply linearly scaled by power due to the non-steady state polymerization kinetics.

4.2. Introduction

Silicone 3D printing has been actively studied due to the good material features such as bio-applicable, corrosion resistive, mechanically elastic and tough, and stable under a high temperature condition [48]. 3D printing processes provide more freedom to fabricate complex geometries, which is challenging to conventional processes such as soft lithography and molding [19, 20]. Various applications have been created such as surgical simulator, tissue engineering, lab-on a chip, and soft robotics [2, 3, 36, 37]. The common 3D printing process for silicone is an extrusion-based process due to a simple system configuration. Using a syringe and nozzle, silicone materials are printed layer by layer. However, the extrusion-based process has disadvantages such as geometrical inaccuracy, poor surface finish, structural defects, and mechanical anisotropy depending on printing orientations [24, 49-51].

To overcome the disadvantages, silicone vat photopolymerization (VP) has been recently studied. A PDMS material system was proposed to print out microchannels with stereolithography (SLA) [9]. An UV-curable silicone for digital light processing (DLP) was developed to realize the similar properties with commercial Sylgard-184 for the lab-on-a-chip application [10]. However, the study showed that the separation force against the inter-bonding between the bottom of the vat and the cured layer were significant. The separation force is one of the major issues for SLA and DLP even with the other polymers [11-13]. The strong adhesion during the separation causes printing failures, structural defects, and even damages on the machine [6]. Various methods have been proposed to solve the separation issue, including non-stick layers, detaching motions, ultrasonic vibrations, chemical inhibition, and optically-created dead zone. Generally, Teflon or PDMS layers as the non-stick layer are applied to the bottom surface of the vat and detaching motions such as sliding, or tilting are used to reduce the separation force [6, 13, 14]. However, the non-stick layers are consumable, and the motions increase the printing time. Ultrasonic vibrations were also proposed to decease the separation force [39]. The vibrations lowered the forces but also created rough surfaces and damages on the small features. The chemical inhibition method was proposed to create a dead zone between the vat bottom and the cured layer [15]. Diffused oxygen gas molecules inhibit the polymerization with certain thickness from the vat bottom. The created dead zone prevents the adhesion between the bottom surface and the cured layer. However, the process is only applicable for the photopolymers with free radical polymerization. The gas diffusion creates a non-uniform distribution of the dead zone and the thin layer of the dead zone slows down the printing speed of large area prints to maintaining the constant level of the oxygen molecules [11]. The oxygen permeable window also has a limited manufacturable size. To overcome the limitations of the chemical inhibition, the authors' previous study proposed the dead zone method with an optical approach [32]. This method created the dead zone by using a low-one photon polymerization (LOPP), regardless of the polymerization types and the limitation of the widow fabrication. A limited curing volume at the focal spot is created by LOPP technique which utilizes a wavelength with a low absorbance rate of the photopolymer and a wide gradient beam [40, 41]. The previous study successful demonstrated the optically created dead zone but also found the slow initiation time, high dimensional variation, and discrepancy between the stationary and moving exposure conditions. The low absorbance rate gave benefits to create the limited curing with the dead zone but also required more time to initiate the polymerization, indicating a slow printing speed and diffusion-dominant condition. The optical array provided the great beam gradient but also generated light refractions or diffractions which made extra exposures in addition to the exposure by the focal spot. The extra exposure caused the high variation and the discrepancy in the process.

This study investigated the ultra-low absorbance wavelength in LOPP to solve the issues from the previous study. The wavelength with a nearly zero absorbance rate was selected to overcome the extra exposure effect and also a high-power source was utilized to shorten the initiation time and to suppress the diffusion condition. To conduct in-depth studies, all the data from this and previous studies were analyzed. For example, the geometrical resolution and variation were evaluated with the experimental study. Actual energy absorptions depending on the wavelength were analyzed to find a relationship with a polymerization behavior. Lastly, using an irradiance model, the discrepancy between the stationary and moving exposure conditions were quantified to evaluate the extra exposure effect.

The paper is organized as follows. Section 2 presents the material and methods including the testbed development with the silicone material, experimental methods, and data analysis approaches. Section 3 explains the results from the experiments and data analysis. This is followed by Section 4, discussion based on the results and comments on the achievements and limitations of this study. The conclusion will be presented at the end of this paper.

4.3. Material and Methods

4.3.1. Testing Material and Experimental Setup

Two set of experiments were conducted with two different exposure conditions: stationary exposure and moving exposure. The former was to observe the dead zone as a function of exposure time, and the later was to observe the dead zone as a function of scanning speed.

This work adopted an UV-curable silicone as the working material, prepared with a methacrylated polydimethylsiloxane (PDMS)-macromer, a 2-Hydroxy-2-methylpropiophenone (2H2M) photoinitiator, and N-vinyl pyrrolidone (NVP) [32]. Figure 24 shows the absorbance spectrum of the photoinitiator measured by a U-4100 spectrophotometer (Hitachi, Tokyo, Japan). The absorbance rates decrease to below 0.4 after 373 nm wavelength. Two wavelengths, 375 nm and 385 nm, have been selected to demonstrate the feasibility of optically created dead zone because of the low absorbance rates. This paper selected a nearly zero absorbance wavelength, 405 nm, with an absorbance rate of 0.006 to characterize and compare its LOPP effects with the published data. Due to an extremely low absorbance, a high power light source is expected to compensate for the time increase.

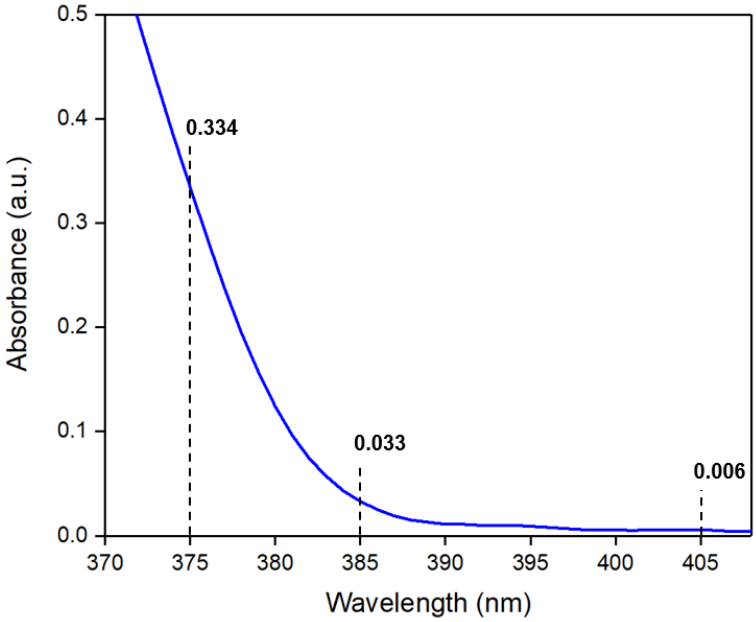

Figure 24. Measured absorbance spectrum of the photoinitiator: each wavelength shows a different absorbance rate (0.334 for 375nm, 0.033 for 385 nm, and 0.006 for 405 nm wavelength).

Figure 25 shows the experimental setup. An industrial 405nm laser module was used as the light source (Sunshine Electronics, Shenzhen, China), which has a specified maximum power of 800 mW. The actual output power was scaled by an Arduino control board. To create a high gradient focusing beam profile, an optical lens array was used, consisting of a plano-concave lens, a plano-convex lens, and a focusing lens (Edmund Optics, Barrington, NJ). The concave lens expands the incident light from the laser module. The convex lens converts the expanded light to a collimated light beam. The focusing lens focuses the beam with the effective focal length (EFL) of 13.0 mm and a numerical aperture of 1 to produce the greatest beam gradient in air. An acrylic resin vat has external dimensions of 25.4 mm by 25.4 mm by 6.3 mm. Three-axis motion stages were controlled by G-codes with a resolution 2.5 µm (Moog Animatics, Milpitas, CA). The light beam after passing the lens array was characterized with a beam profiler (Edmund Optics, Barrington, NJ) and a power meter (Edmund Optics, Barrington, NJ) to ensure the beam condition. The beam profile followed a Gaussian distribution (80.7% fitness) with a diameter of 0.4 mm defined by the width at $1/e^2$ of the peak intensity. The maximum power was measured to be 591 mW after the lens array.

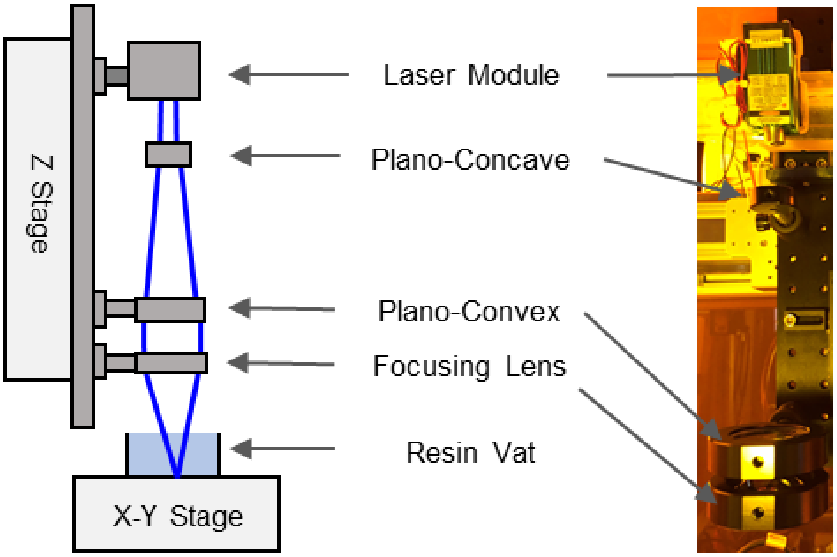

Figure 25. Details for the optical lens array of the experimental setup.

4.3.2. Experimental Methods

Two different exposure conditions, stationary and moving exposures, were tested to observe the growth of curing and the actual printing, as shown in Figure 26 (a) and (b) schematically. In these tests, the vat was filled with the silicone resin, and the focal spot of the beam was set at the vat bottom to create the dead zone from the liquid surface. The size of the cured structure is expected to be a function of time (and scanning speed for the moving condition).

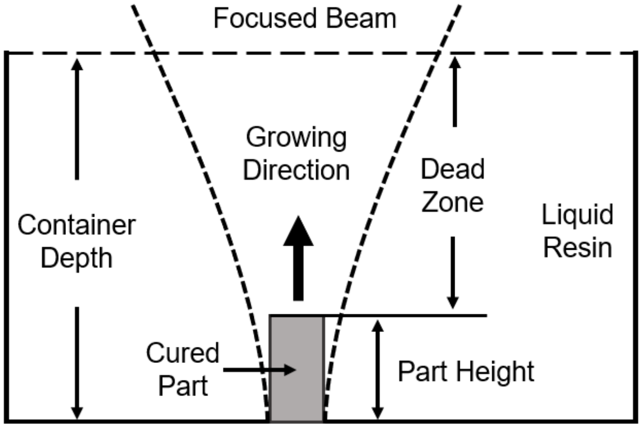

(a)

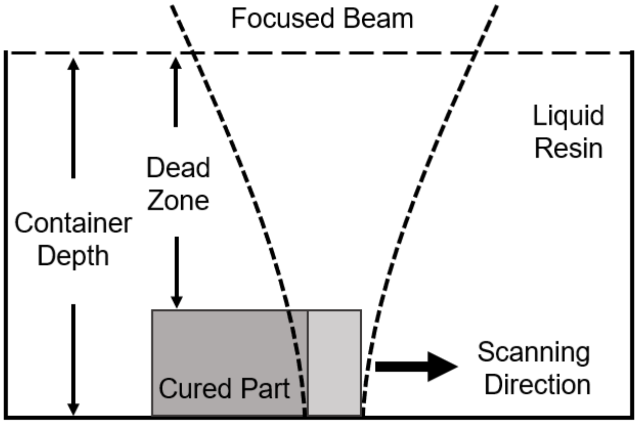

(b)

Figure 26. Schematic of the experimental studies: (a) stationary exposure test, (b) moving exposure test.

In the stationary condition, different exposure times were tested. The first observable cure was marked as the initiation time, where the polymerization starts. This time indicates the fastest printing speed needed to form a solid structure. Then, the sample heights of different exposure times were recorded to represent the growth rate, which describes how sensitive the cure is to the time. The smaller growth rate means an easier control over the cure size.

In the prior study, two wavelengths 375 nm and 385 nm were used, and the initiation time was in the range of 100 - 200 s with the selected powers. In this study, the power selection of the 405 nm laser was aimed to reach a similar initiation time for a comparative analysis. Based on the trials and errors, 400 mW was found to fall in a reasonable range. Another two power levels, 200 mW and 600 mW were added to the experiment matrix. Table 6 shows the planned and actual beam powers detected by the power meter.

Table 6 A single-variable experiment for the stationary exposure test

Planned power	**Actual power for 405 nm**
200 mW	196 mW
400 mW	395 mW
600 mW	591 mW

Using the 400 mW power, moving exposure condition was tested with six different scanning speeds to observe the consistency of the printed structure, as listed in Table 7. Similarly, the focal spot of the beam was set at the vat bottom and moved from left to right with a constant scanning speed. The dimensions of the cured parts were measured to evaluate the dead zone formation, printing accuracy and resolution.

Table 7 Six scanning speeds for the moving exposure test

Wavelength	**405 nm**
Scanning speed (mm/min)	0.21, 0.23, 0.28, 0.35, 0.42, 0.50

4.3.3. Data Analysis Approaches

4.3.3.1. Geometrical Resolution and Variation

Two metrics used to indicate the resolution and geometrical consistency of the print are the growth rate in the stationary exposure test and the height variation in the moving exposure test. The growth rate is determined by a least square linear fit through all points of different exposure times. The slope indicates the speed of the cure grows over time on an average. These data are compared to the published data with 375 nm and 385 nm wavelength. For example, the 375 nm wavelength with a beam power of 3.6 mW generated a growth rate of 0.91 mm/s, whereas the 385 nm at a similar power (3.4 mW) produced a growth rate of 0.0015 mm/s. On the other hand, if scaling the 385 nm power (11.3 mW) to reach a similar initiation time, the growth rate becomes 0.095 mm/s. Both indicate the longer wavelength has a better control. The result of 405 nm will be included in the comparison to see the effect of an ultra-low absorbance.

For the moving exposure test, the heights of the cured linear structure are measured in multiple cross-sections across the length. The prior data showed that 375 nm cannot effectively create a linear structure under the liquid surface due to the inability of creating a wide dead zone. The 385 nm wavelength shows a noticeable variation of 0.11 mm with an average height of 1.6 mm even in the optimal scanning speed. The results of 405 nm are included to see whether there is improvement.

4.3.3.2. Exposure Equivalency

Exposure equivalency in the context of this study means that the polymerization is identical when photopolymers absorb the same amount of photon energy, regardless of the wavelength. It also means that the light power and exposure time can be scaled linearly. That is, a doubled power has the same effect as that of a doubled exposure time. The existence of exposure equivalency is critical to understand whether the printing time can be shortened effectively by the light power.

For this, the stationary test results can be converted from a function of exposure time (t) to a function of the true exposure (E_{true}) by Eq. (1), where A is the photoinitiator absorbance rate at a given wavelength and I is the irradiance in the unit of mW/mm^2.

$$E_{true} = I \times A \times t \quad (1)$$

The irradiance within the focusing spot is a Gaussian distribution, so the maximum value (at the center of the focusing spot) can be expressed by Eq (2), where W_0 is the radius of the Gaussian beam and P_L is the power of the light. Note that W_0 was measured by a beam profiler with the $1/e^2$ width definition; P_L was measured by a power meter.

$$H = \frac{2P_L}{\pi {W_0}^2} \quad (2)$$

Table 8 below shows the true irradiance value at the center of the focal spot for 405 nm wavelength as well as the previous published data for 375 and 385 nm. 405 nm wavelength shows much higher irradiances due to higher beam powers and smaller beam diameters, in spite of the smaller absorbance rate. To achieve the similar initiation time between 385nm and 405 nm wavelengths, at least 47 times higher true irradiance is required for 405 nm wavelength. The relationships between the cured height and actual exposure will be plotted together to verify the exposure equivalency across these wavelengths.

Table 8 True irradiances for 375 nm, 385nm, and 405 nm wavelength

Wavelength	**Absorbance rate [A.U.]**	**Beam diameter [mm]**	**Beam power [mW]**	**Irradiance [mW/mm^2]**	**True irradiance [mW/mm^2]**
375	0.334	1.1	2.3	4.8	1.6
			3.6	7.6	2.5
385	0.033	1.1	3.4	7.2	0.2
			11.3	23.8	0.8
405	0.006	0.4	395	6286	37.7
			591	9406	56.4

4.3.3.3. Extra-Exposure Effect

For a fixed light source, the level of curing should be identical in both stationary and moving conditions when the exposures are the same. While in several prior works [32, 42, 43], it was found that the moving condition needed much less exposure to achieve curing. This discrepancy is likely due to an extra-exposure effect, which is caused by light refraction or diffraction in the optical array during a long scanning time. To more precisely determine the effect, the term exposure difference (ED%) is defined to describe the difference between the moving exposure (E_{mov}) and stationary exposure (E_{stat}) when the first curing spot is observed, as shown in Eq. (3). ED% should be theoretically zero when the extra-exposure effect does not exist.

$$ED\% = \frac{E_{mov} - E_{stat}}{E_{stat}} \times 100\% \quad (3)$$

The exposures can be derived from the irradiance under the liquid considering a light source of Gaussian distribution, beam gradient, and attenuation by the resin. The light source can be expressed by Eq. (4), where W_0 is the radius of the Gaussian beam and H_0 is the maximum irradiance based on the power of the light P_L, so that $H_0 = \frac{2P_L}{\pi {W_0}^2}$.

$$H(x,y) = H_0 \cdot e^{-2x^2/{W_0}^2} e^{-2y^2/{W_0}^2} \quad (4)$$

After the focusing lens, the beam converges towards the focal spot and the beam diameter changes along the axial direction (denoted by W_z) as shown in Figure 27. Therefore, Eq. (4) can be generalized to Eq. (5) while the total beam power remains the same, such that $H_z = \frac{2P_L}{\pi {W_z}^2}$.

$$H(x,y) = H_z \cdot e^{-2x^2/{W_z}^2} e^{-2y^2/{W_z}^2} \qquad (5)$$

The attenuation is the consequence of light absorption by the liquid resin, which can be described as an exponential decade along the depth by Beer-Lambert law [52]. This further transforms Eq. (5) to the following form,

$$H(x,y,z) = \frac{2P_L}{\pi {W_z}^2} \cdot e^{-2x^2/{W_z}^2} e^{-2y^2/{W_z}^2} e^{-Z/D_p} \qquad (6)$$

where D_p is the penetration depth of the liquid resin at which the irradiance decades to *1/e* (about 37%). The attenuation can distort the beam profile along the depth. The penetration depth can be obtained by a direct measurement method with the power meter [53].

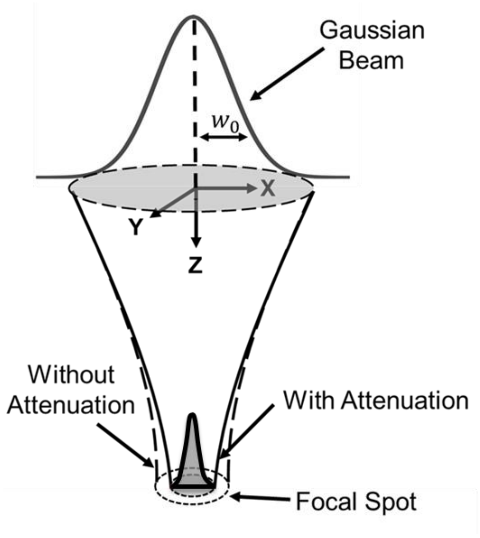

Figure 27. A schematic of the irradiance model.

Considering the middle plane of the Gaussian beam (i.e., y = 0), the total exposure can be calculated by multiplying the exposure time (*t*), such that

$$E(x,z,t) = \frac{2P_L}{\pi {W_z}^2} \cdot t \cdot e^{-2x^2/{W_z}^2} e^{-Z/D_p} \qquad (7)$$

Since the exposure is not uniform across the focal spot, an average exposure is used, as shown by Eq. (8), where the depth (Z) is substituted with 5 mm on the vat bottom.

$$E_{stat} = \frac{\mathrm{Erf}(\sqrt{2})P_L}{\sqrt{2\pi}{W_0}^2} \cdot t \cdot e^{-5/D_p} \ (8)$$

For the beam scanning with a constant velocity $v_{S.}$ along the x axis, the total exposure is expressed by Eq. (8). Note the exposure is constant across the scanning length.

$$E_{mov} = \sqrt{\frac{2}{\pi}} \cdot \frac{P_L}{W_z V_S} \cdot e^{-5/D_p} \quad (9)$$

4.4. Results

4.4.1. Resolution and Geometrical Variation

4.4.1.1. Stationary Exposure Test

Three different beam powers of 196 mW, 395 mW, and 591 mW were tested. Since the 196 mW light could not cure the material over 300 s, it was noted NA in the experiment. The other two beam powers (395 mW and 591 mW) were found to start the curing at 100 s and 45 s, respectively. Figure 28 shows physical samples from the stationary exposure test with the beam powers of 395 mW and 591 mW. As the exposure time increased, the cured parts grew from a bottom disc to the tip upward. This is because the Gaussian distributed light produces the highest exposure at the center. Figure 29 shows the measured heights against the exposure time for both 395 mW and 591 mW. Error bars represent one standard deviation from the measured data. With the beam power of 395 mW, the exposure time was tested from 60 s to 480 s. The first observable curing was found at 100 s with a height of 0.209 mm. This indicates a large dead zone (about 4.791 mm) and fine resolution. Between 100 s and 480 s, the linear fitted trend line represents a vertical growth rate of the cured part, which is about 0.0026 mm/s. For the results with the beam power of 591 mW, the exposure time was tested from 15 s to 140 s. The first observation of curing was shortened to 45 s with a height of 0.213 mm. Between 45 s and 140 s, the vertical growth rate was 0.0035 mm/ s. Compared to the data of 395 mW, the results of 591 mW showed about twice shorter initiation time but a similar growth rate. This indicates that at this wavelength, the power can effectively reduce the initiation time without sacrificing the controllability of the resolution.

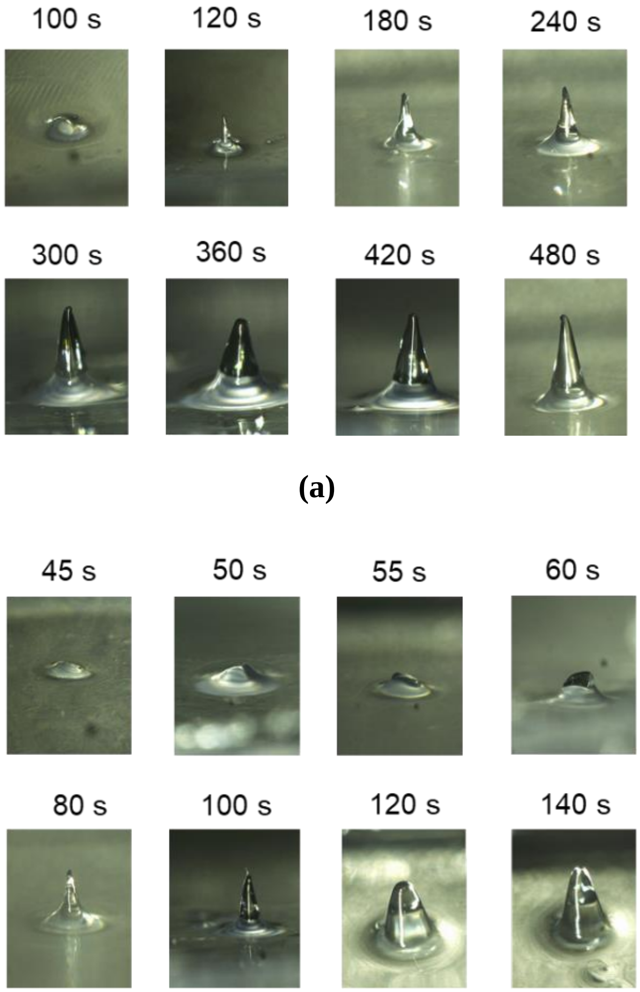

(a)

(b)

Figure 28. Physical samples from the stationary exposure tests with 405 nm wavelength: (a) beam power of 395 mW (exposure time: 100 s ~ 480 s), (b) beam power of 591 mW (exposure time: 45 s ~ 140 s).

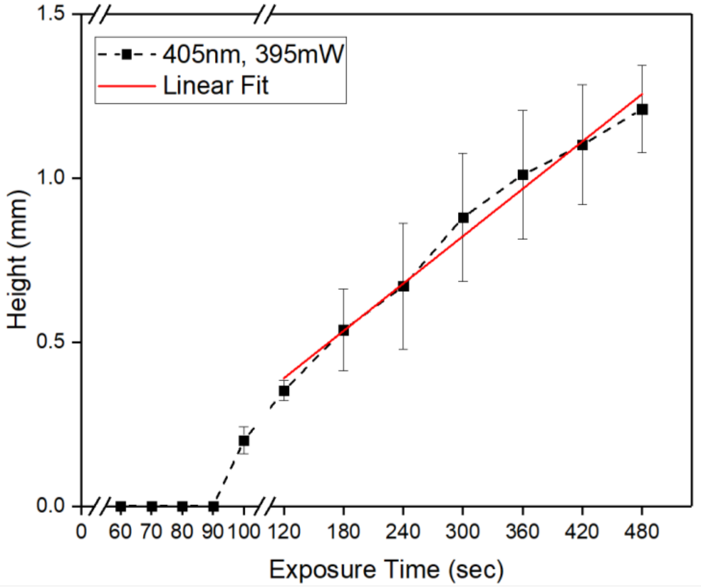

(a)

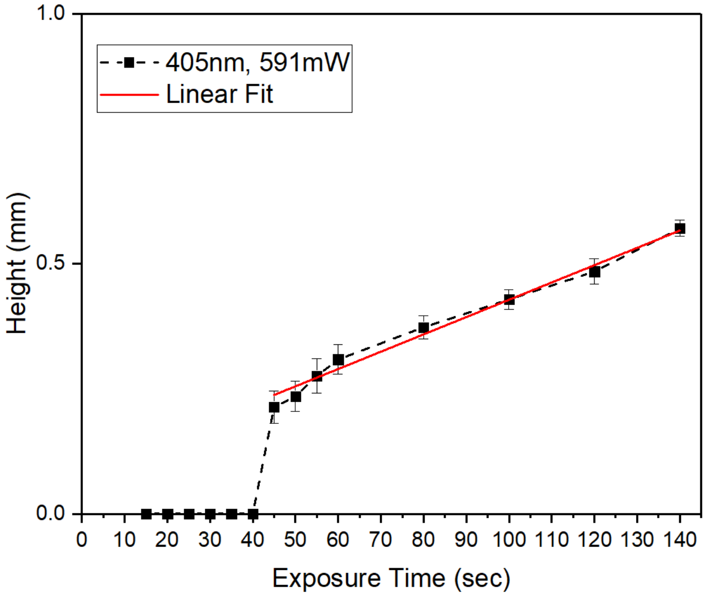

(b)

Figure 29. Results of the stationary exposure test with 405 nm wavelength: beam power of 395 mW (exposure time: 60 s ~ 480 s), (b) beam power of 591 mW (exposure time: 15 s ~ 140 s). The error bars represent the standard deviation of the measured heights.

Figure 30 summarize the results of the initiation times and growth rates of 375 nm, 385 nm, and 405 nm wavelengths, from the published and current studies. As seen, 405 nm wavelength produces a very low growth rate compared to those of 375 nm and 385 nm with a comparable initiation time. Quantitatively, by comparing the maximum powers for each wavelength, 405 nm wavelength has a growth rate at least 27 times slower than the other two. This means that it is much easier to control the dead zone and resolution.

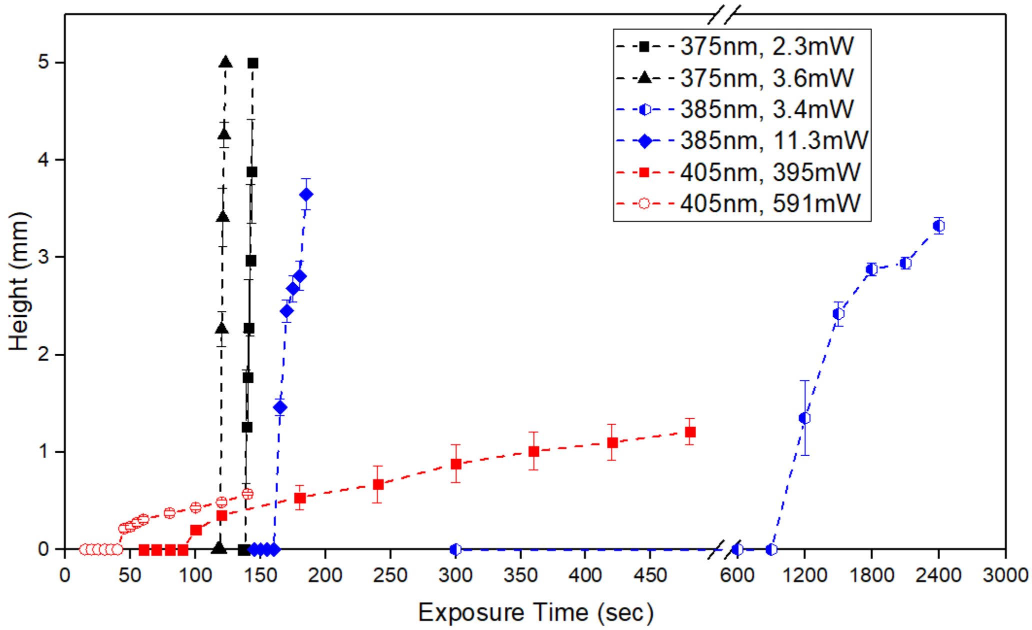

Figure 30. Results of the stationary exposure test with 375 nm, 385 nm, and 405 nm wavelength.

4.4.1.2. Moving Exposure Test

Six different scanning speeds were tested, but only three scanning speeds (0.21 mm/min, 0.23 mm/min, and 0.28 mm/min) could cure the resin. The actual images are shown in Figure 31. The cured parts had a wall-shape structure with upright position. The parts mostly show a uniform height and width, but the length of the structures dramatically decreases (away from the nominal 20 mm length) as the scanning speed increases. This is because none or incomplete curing might occur at the beginning at the faster feed rates.

To quantify geometrical variations, the structure height was measured several times across the length and plotted together with the published results of 375 and 385 nm on Figure 32. In comparison, the 405 nm wavelength produces a much smaller height with lower variation than those in shorter wavelengths. By comparing the fastest, curable scanning speed for each wavelength (highlighted box in Figure 32), 405 nm wavlength produced at least five times smaller height (0.28 mm) than the height of 385 nm wavlength (1.6 mm). This further shows a high resolution and stable dead zone (at least 4.5 mm) for the 405 nm wavelength. Note 375 nm was not included in the comparison as the cured structures were too close to the liquid surface, which intefered the height.

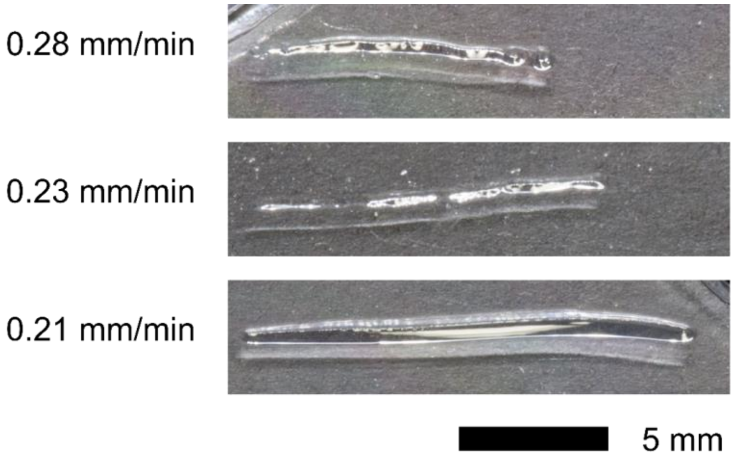

Figure 31. Physical samples from the moving exposure tests with 405 nm wavelength and different scanning speeds of 0.28 mm/min, 0.23 mm/min, and 0.21 mm/min.

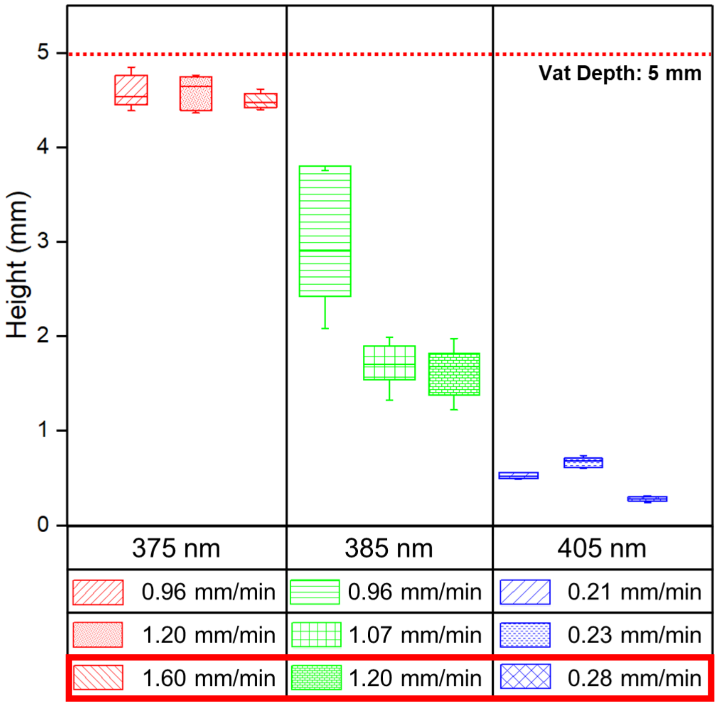

Figure 32. Heights in the moving exposure test with different scanning speeds of 375 nm, 385 nm, and 405 nm wavelength.

4.4.2. Evaluation for Exposure Equivalency

Figure 33 is a converted chart of Figure 30 with the true irradiance in Table 8. The data points of no curing are excluded. The dispersed data points of all wavelengths indicate that exposure equivalency does not exist in LOPP. In particular for the 405 nm wavelength, it requires at least ten times higher exposure to cure the resin. In other words, in addition to compensate the low absorbance of 405 nm, more beam power or time is needed. For example, to achieve a similar initiation time of 375 nm wavelength, 405 nm required 500 times higher power, in which 50 times accounts for the absorbance difference (0.334 vs. 0.006) and 10 times accounts for the difference in the initial exposure (300 vs. 3000 mJ/mm^2). This can be a serious barrier in practical use.

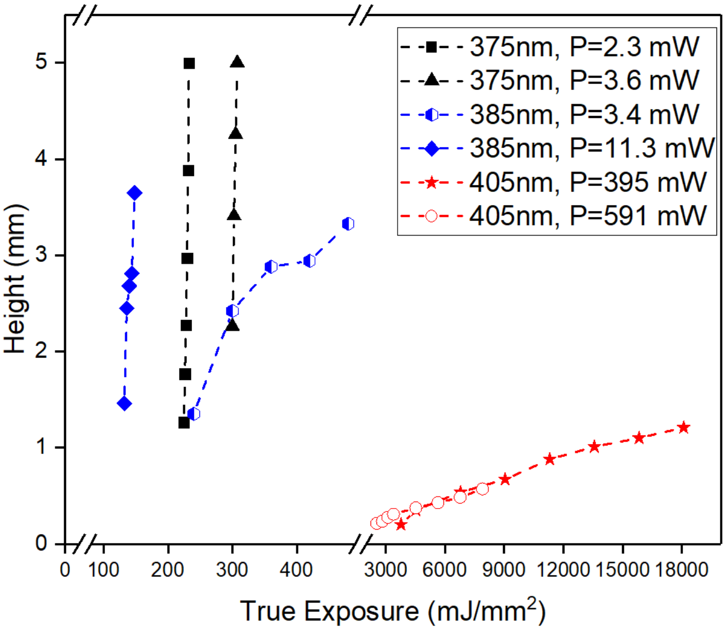

Figure 33. True exposure vs heights of the stationary exposure test with 375 nm, 385 nm, and 405 nm wavelength.

4.4.3. Extra-Exposure Effect

The extra-exposure effect is evaluated by ED% using the exposure with the initiation time in the stationary exposure test and the exposure with the fastest curable scanning speed in the moving exposure test. Table 9 shows all the parameters for the equations and computation results for all 375 nm, 385 nm, and 405 nm wavelengths. The 405 nm wavelength shows a high penetration depth due to the low absorbance rate, and also a low ED% of -9 %. On the other hand, 375 nm and 385 nm wavelength show much greater ED% values (-64 % and -65 %). This indicates that the extra-exposure effect is noticeable in 375 nm and 385 nm, while it is small in 405 nm (-9%), indicating that the absorbance may be too low to reach any curing threshold despite the extra-exposure. This is a positive result because, in this case, the stationary test can be used to plan the printing speed and size.

Table 9 Modeling parameters for the numerical analysis and differences between the stationary and moving exposure conditions with 375 nm, 385 nm, and 405 nm wavelengths

Wavelength [nm]	**Power [mW]**	**Beam diameter [mm]**	**Penetration depth [mm]**	**Initiation time [sec]**	**Fastest curable scanning speed [mm/min]**	**Exposure difference [%]**
375	3.6	1.1	18	120	1.6	- 64
385	11.3	1.1	236	165	1.2	- 65
405	395	0.4	912	100	0.28	- 9

In additional to compare the initial curing time (and speed), the same analysis can also be applied to compute the exposures for a certain height and observe the differences. Figure 34 shows the cured height against the true exposure for 375nm, 385nm, and 405nm. The results of 375 nm and 385 nm show obvious discrepancy between the stationary and moving exposures. Specifically, in 385 nm wavelength, smaller exposure levels cured the material under the moving exposure condition due to the extra-exposure effect. In 375 nm wavelength, constantly great cured heights in the moving condition were found compared to the ones in the stationary condition, indicating more sensitive to the extra-exposure effect due to a higher absorbance rate. On the other hand, 405 nm wavelength shows the similar exposure levels between the stationary and moving exposure conditions. It again proves that the extra-exposure is less effective with 405 nm wavelength due to a nearly zero absorbance rate.

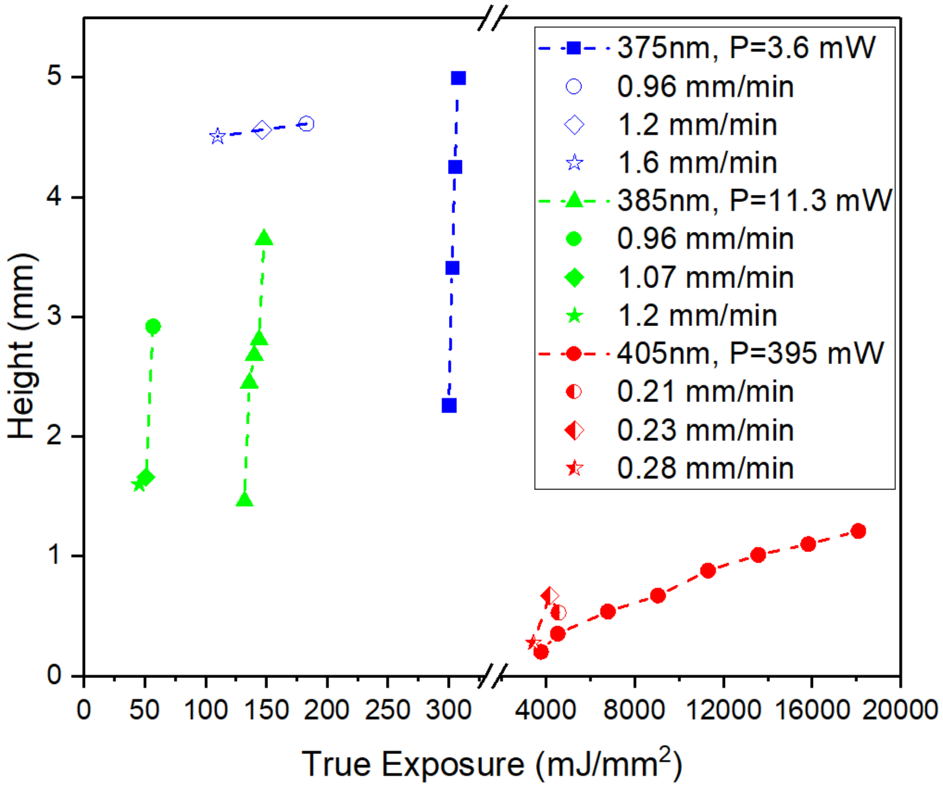

Figure 34. True exposure vs heights for the stationary test and the exposure test of all the wavelength.

4.5. Discussion

This study successfully demonstrated a higher curing resolution and lower geometrical variation with 405 nm wavelength. The ultra-low absorbance wavelength provided a small curing volume with a slow growth rate, which indicates a much easier control over the curing process with a large dead zone. However, the use of 405 nm wavelength poses a major concern in printing time. It requires approximately 10 times higher true exposure to cure the material than 375 nm and 385 nm wavelengths. In other words, by including the absorbance difference, the power requirement could be a few hundred times higher for 405 nm to achieve a similar printing time to that of 385 or 375 nm. This exposure in-equivalency is likely caused by an unsteady-state polymerization due to low photon absorption. Usually, the steady state polymerization has equal initiation rate to termination rate, by which the transformation rate is linearly proportional to the time and irradiance. An unsteady-state process is more affected by polymer kinetics such as decomposition of the photoinitiator, initiation and propagation of the networking, and conversion efficiency of the material system.

Although the high power requirement presents a practical difficulty, it can be technically addressed by a high-power laser source, a small beam diameter (to increase irradiance), or multiple light sources, while these can also raise safety concerns. Alternatively, a slightly shorter wavelength between 385 nm and 405 nm wavelengths may be used to compromise between printing quality and time. Nonetheless, it is obvious that an ideal LOPP-based printing exists in a very narrow wavelength window.

Regarding the extra-exposure effect, the discrepancy between the stationary and moving exposure tests was observed with all the wavelengths. The long testing time in the moving exposure test causes the less exposure area to initiate the polymerization process due to additional exposure in the testing environment. However, 405 nm wavelength was less sensitive to the extra-exposure effect because of its ultra-low absorbance. This is beneficial as the printing process can now be calibrated by a simple stationary exposure condition.

4.6. Conclusions

This study investigated the ultra-low absorbance wavelength in LOPP for the silicone dead zone process. In terms of geometrical resolution and variation, exposure equivalency, and extra-exposure effect, the experiments and data analysis were designed and conducted. The 405 nm wavelength showed a high printing resolution and low geometrical variation thanks to the nearly zero absorbance rate. However, 405 nm wavelength required much higher irradiance to compensate the low absorbance rate. The exposure equivalency was not found. Each wavelength showed different polymerization behaviors. Especially, 405 nm wavelength required the different exposure range due to the higher irradiances or the longer exposure times. The extra-exposure effect was not significant to 405 nm wavelength. This provided a small discrepancy between the stationary and moving exposure test. The irradiance model quantified the difference of -9 % for 405 nm wavelength, compared to -64 % and -65 % for 375nm and 385 nm wavelength respectively. As future works, two major tasks could be considered: beam and material optimizations. Different wavelengths between 385 nm and 405 nm wavelength could be tested to find a reasonable irradiance level with obtaining a good resolution and low variation. Due to the limitation for available light sources, material system could be optimized with different concentrations or even different photoinitiators. In addition, different photocuring process such as cation polymerization could be tested to demonstrate the versality of this process.

5. CONCLUSIONS AND FUTURE WORKS

5.1. Conclusions and Major Contributions

This dissertation studied the silicone stereolithography with an optically created dead zone to solve the separation force in a conventional VP process. The DLP printer was utilized to characterize the printability of the silicone photopolymer. The mechanical isotropy and postcure shrinkage were evaluated. The optically created dead zone process was also investigated with an experimental and numerical methods.

Major contributions of this dissertation can be summarized as follows:

I. The printability of the silicone was demonstrated with a commercial DLP printer. Using the optimized printing parameters, good dimensional accuracies were achieved with an average error of 1.3%. The printed PDMS showed high directionality in the modulus, elongation, and strength due to the layering direction and printing time. Minimal postcure shrinkages were achieved with the average shrinkage rate of 0.3%. Despite a successful demonstration of PDMS printing, the separation issue in DLP remains challenging and requires further research and development to overcome.

II. The results of 375 nm, 385 nm, and 405 nm wavelength showed that a dead zone was produced through the LOPP effect, while different wavelengths resulted in drastically different initiation times, growth rates, and resulting cured shapes. The 375 nm wavelength presented a shorter initiation time, a faster growth rate, and a larger shape, indicating a faster printing but worse resolution. The dead zone was also not that obvious. On the other hand, the 385 nm wavelength produced a fine resolution and a large, stable dead zone due to a slower growth rate. However, the initiation time for 385 nm is much longer. Lastly, the 405 nm wavelength presented a shorter initiation time and also a slower growth rate to increase the curing speed and to obtain the stable process.

III. With the Gaussian distribution, 405 nm wavelength achieved a much smaller error of 9% and the other wavelengths showed three time decreases in error. The uniform distribution gave huge errors of 191%, 200%, and 33% respectively. Especially the bigger beam diameter of 375 nm and 385 nm wavelength increased the differences between the actual beam distribution and the assumed distribution.

IV. The optical aberration and diffraction cause the additional exposing area beside the focusing spot. The long experiment time in a scanning process causes additional exposure to the entire resin. This issue may be minimized by a shorter experiment time with a higher beam power and a narrow and well-defined beam focusing spot.

5.2. Future Works

The proposed silicone 3D printing process with optically created dead zone and the numerical model can be improved. Future research can follow the following directions:

I. The proposed dead zone process can be scaled with the high-beam power. In the future, the applicable high-power source will be considered to check the practical limitations of the process. In addition, applicable printing scale will be evaluated in terms of printing time and printing costs

II. This study proved that the higher resolution and low dimensional variation can be achieved with the wavelength of nearly zero absorbance rate. In the future, in-depth analysis will be conducted to characterize the printing quality. Some geometries will be printed to verify the limitations and challenges of the process.

III. The irradiance model quantified the discrepancy between the stationary and moving exposure conditions. In the future, additional extraneous factors such as the light refraction or diffraction from the optical array could be plugged into the model to improve the accuracy of the results.

IV. This study demonstrated the printability of PDMS with a commercial DLP printer. The separation issue was critical to the DLP process. In the future, the separation force can be quantified with a force sensor and some design of the experiments.

REFERENCES

1. Muroi, H., et al., *Development of Optical 3D Gel Printer for Fabricating Free-Form Soft & Wet Industrial Materials and Evaluation of Printed Double-Network Gels.* Journal of Solid Mechanics and Materials Engineering, 2013. **7**(2): p. 163-168.
2. Laurent, M., et al., *Clinical evaluation of the marginal fit of cast crowns – validation of the silicone replica method.* Journal of Oral Rehabilitation, 2008. **35**(2): p. 116-122.
3. Place, E.S., et al., *Synthetic polymer scaffolds for tissue engineering.* Chemical Society Reviews, 2009. **38**(4): p. 1139-1151.
4. Roche, E.T., et al., *A Bioinspired Soft Actuated Material.* Advanced Materials, 2014. **26**(8): p. 1200-1206.
5. Kang, H.-W. and D.-W. Cho, *Development of an Indirect Stereolithography Technology for Scaffold Fabrication with a Wide Range of Biomaterial Selectivity.* Tissue Engineering. Part C, Methods, 2012. **18**(9): p. 719-729.
6. Liravi, F., S. Das, and C. Zhou, *Separation force analysis and prediction based on cohesive element model for constrained-surface Stereolithography processes.* Computer-Aided Design, 2015. **69**: p. 134-142.
7. Truby, R.L. and J.A. Lewis, *Printing soft matter in three dimensions.* Nature, 2016. **540**: p. 371.

8. Plott, J. and A. Shih, *The extrusion-based additive manufacturing of moisture-cured silicone elastomer with minimal void for pneumatic actuators.* Additive Manufacturing, 2017. **17**: p. 1-14.

9. Au, A.K., W. Lee, and A. Folch, *Mail-order microfluidics: evaluation of stereolithography for the production of microfluidic devices.* Lab on a Chip, 2014. **14**(7): p. 1294-1301.

10. Bhattacharjee, N., et al., *Desktop-Stereolithography 3D-Printing of a Poly(dimethylsiloxane)-Based Material with Sylgard-184 Properties.* Advanced Materials, 2018. **30**(22): p. 1800001.

11. Pan, Y., et al., *Study of separation force in constrained surface projection stereolithography.* Rapid Prototyping Journal, 2017. **23**(2): p. 353-361.

12. He, H., et al., *Effect of Constrained Surface Texturing on Separation Force in Projection Stereolithography.* Journal of Manufacturing Science and Engineering, 2018. **140**(9): p. 091007-091007-9.

13. Huang, Y.-M. and C.-P. Jiang, *On-line force monitoring of platform ascending rapid prototyping system.* Journal of Materials Processing Technology, 2005. **159**(2): p. 257-264.

14. Pan, Y., C. Zhou, and Y. Chen, *A Fast Mask Projection Stereolithography Process for Fabricating Digital Models in Minutes.* Journal of Manufacturing Science and Engineering, 2012. **134**(5): p. 051011-051011.

15. Tumbleston, J.R., et al., *Continuous liquid interface production of 3D objects.* Science, 2015. **347**(6228): p. 1349-1352.

16. Zhang, Y., et al., *Printing, folding and assembly methods for forming 3D mesostructures in advanced materials.* Nature Reviews Materials, 2017. **2**: p. 17019.

17. Timmer, M.D., et al., *Fabrication of poly(propylene fumarate)-based orthopaedic implants by photo-crosslinking through transparent silicone molds.* Biomaterials, 2003. **24**(25): p. 4707-4714.

18. Chang, S.C.N., et al., *Injection molding of chondrocyte/alginate constructs in the shape of facial implants.* Journal of Biomedical Materials Research, 2001. **55**(4): p. 503-511.

19. Park, J.-H., et al., *Polymer particle-based micromolding to fabricate novel microstructures.* Biomedical Microdevices, 2007. **9**(2): p. 223-234.

20. Lord, H.A. and G. Williams, *Mold-filling studies for the injection molding of thermoplastic materials. Part II: The transient flow of plastic materials in the cavities of injection-molding dies.* Polymer Engineering & Science, 1975. **15**(8): p. 569-582.

21. Duoss, E.B., et al., *Three-Dimensional Printing of Elastomeric, Cellular Architectures with Negative Stiffness.* Advanced Functional Materials, 2014. **24**(31): p. 4905-4913.

22. McCoul, D., et al., *Inkjet 3D printing of UV and thermal cure silicone elastomers for dielectric elastomer actuators.* Smart Materials and Structures, 2017. **26**(12): p. 125022.

23. Muthusamy, M., S. Safaee, and K.R. Chen, *Additive Manufacturing of Overhang Structures Using Moisture-Cured Silicone with Support Material.* Journal of Manufacturing and Materials Processing, 2018. **2**(2).

24. Plott, J., X. Tian, and A.J. Shih, *Voids and tensile properties in extrusion-based additive manufacturing of moisture-cured silicone elastomer.* Additive Manufacturing, 2018. **22**: p. 606-617.

25. Hague, R., et al., *Materials analysis of stereolithography resins for use in Rapid Manufacturing.* Journal of Materials Science, 2004. **39**(7): p. 2457-2464.

26. Dulieu-Barton, J.M. and M.C. Fulton, *Mechanical Properties of a Typical Stereolithography Resin.* Strain, 2000. **36**(2): p. 81-87.

27. Bártolo, P.J., *Stereolithography: materials, processes and applications*. 2011: Springer Science & Business Media.

28. Jacobs, P.F. *Fundamentals of stereolithography*. in *The Solid Freeform Fabrication Symposium*. 1992. Austin, Texas.

29. Karalekas, D. and A. Aggelopoulos, *Study of shrinkage strains in a stereolithography cured acrylic photopolymer resin.* Journal of Materials Processing Technology, 2003. **136**: p. 146-150.

30. Jacobs, P.F., *Rapid prototyping & manufacturing: fundamentals of stereolithography*. 1992: Society of Manufacturing Engineers.

31. Monzón, M., et al., *Anisotropy of Photopolymer Parts Made by Digital Light Processing.* Materials (Basel, Switzerland), 2017. **10**(1): p. 64.

32. Kim, D.S., et al., *Feasibility study of silicone stereolithography with an optically created dead zone.* Additive Manufacturing, 2019. **29**: p. 100793.

33. Femmer, T., A.J.C. Kuehne, and M. Wessling, *Print your own membrane: direct rapid prototyping of polydimethylsiloxane.* Lab on a Chip, 2014. **14**(15): p. 2610-2613.

34. Dikova, T., et al., *Dimensional accuracy and surface roughness of polymeric dental bridges produced by different 3D printing processes.* Archives of Materials Science and Engineering, 2018. **2**: p. 65-75.

35. Ligon, S.C., et al., *Polymers for 3D Printing and Customized Additive Manufacturing.* Chemical reviews, 2017. **117**(15): p. 10212-10290.

36. Rossiter, J., P. Walters, and B. Stoimenov, *Printing 3D dielectric elastomer actuators for soft robotics*. SPIE Smart Structures and Materials + Nondestructive Evaluation and Health Monitoring. Vol. 7287. 2009: SPIE.

37. Kim, D.S., et al., *An efficient 3-dimensional hydrodynamic focusing microfluidic device by means of locally increased aspect ratio.* Microelectronic Engineering, 2009. **86**(4): p. 1343-1346.

38. A., P.D., et al., *Additive Manufacturing with Ultraviolet Curable Silicones Containing Carbon Black.* 3D Printing and Additive Manufacturing, 2018. **5**(1): p. 73-86.

39. Jin, J., et al., *A vibration-assisted method to reduce separation force for stereolithography*. Journal of Manufacturing Processes, 2018. **34**: p. 793-801.

40. Li, Q., et al., *Concept for three-dimensional optical addressing by ultralow one-photon absorption method.* Optics Letters, 2013. **38**(22): p. 4640-4643.
41. Do, M.T., et al., *Submicrometer 3D structures fabrication enabled by one-photon absorption direct laser writing.* Optics Express, 2013. **21**(18): p. 20964-20973.
42. Kim, D.S. and B.L. Tai, *Hydrostatic support-free fabrication of three-dimensional soft structures.* Journal of Manufacturing Processes, 2016. **24**: p. 391-396.
43. Kim, D.S., Y.-T. Kao, and B.L. Tai, *Hydrostatic 3D-printing for soft material structures using low one-photon polymerization.* Manufacturing Letters, 2016. **10**: p. 6-9.
44. Husár, B., et al., *The formulator's guide to anti-oxygen inhibition additives.* Progress in Organic Coatings, 2014. **77**(11): p. 1789-1798.
45. Miller, C.W., et al., *N-Vinylamides and Reduction of Oxygen Inhibition in Photopolymerization of Simple Acrylate Formulations*, in *Photoinitiated Polymerization*. 2003, American Chemical Society. p. 2-14.
46. Buback, M. and A.M. van Herk, *Radical polymerization: kinetics and mechanism*. 2007: John Wiley & Sons.
47. Korolyov, G.V. and M. Mogilevich, *Three-dimensional free-radical polymerization: cross-linked and hyper-branched polymers*. 2008: Springer Science & Business Media.
48. and, Y.X. and G.M. Whitesides, *SOFT LITHOGRAPHY.* Annual Review of Materials Science, 1998. **28**(1): p. 153-184.

49. Hamidi, A., S. Jain, and Y. Tadesse, *3D printing PLA and silicone elastomer structures with sugar solution support material*. SPIE Smart Structures and Materials + Nondestructive Evaluation and Health Monitoring. Vol. 10163. 2017: SPIE.

50. Ippolito, R., L. Iuliano, and A. Gatto, *Benchmarking of Rapid Prototyping Techniques in Terms of Dimensional Accuracy and Surface Finish.* CIRP Annals, 1995. **44**(1): p. 157-160.

51. Ahn, S.H., *Anisotropic material properties of fused deposition modeling ABS.* Rapid Prototyping Journal, 2002. **8**(4): p. 248-257.

52. Beer, *Determination of the absorption of red light in colored liquids.* Annalen der Physik und Chemie, 1852. **86**: p. 78–88.

53. Onorato, P., et al., *The Beer Lambert law measurement made easy*. Physics Education, 2018. **53**(3): p. 035033.